Continuum Mech. Thermodyn. (2018) 30:421–455
https://doi.org/10.1007/s00161-017-0604-8

ORIGINAL ARTICLE

J. D. Clayton · J. Knap

Continuum modeling of twinning, amorphization, and fracture: theory and numerical simulations

Received: 27 July 2017 / Accepted: 6 November 2017 / Published online: 14 December 2017

Abstract A continuum mechanical theory is used to model physical mechanisms of twinning, solid-solid phase transformations, and failure by cavitation and shear fracture. Such a sequence of mechanisms has been observed in atomic simulations and/or experiments on the ceramic boron carbide. In the present modeling approach, geometric quantities such as the metric tensor and connection coefficients can depend on one or more director vectors, also called internal state vectors. After development of the general nonlinear theory, a first problem class considers simple shear deformation of a single crystal of this material. For homogeneous fields or stress-free states, algebraic systems or ordinary differential equations are obtained that can be solved by numerical iteration. Results are in general agreement with atomic simulation, without introduction of fitted parameters. The second class of problems addresses the more complex mechanics of heterogeneous deformation and stress states involved in deformation and failure of polycrystals. Finite element calculations, in which individual grains in a three-dimensional polycrystal are fully resolved, invoke a partially linearized version of the theory. Results provide new insight into effects of crystal morphology, activity or inactivity of different inelasticity mechanisms, and imposed deformation histories on strength and failure of the aggregate under compression and shear. The importance of incorporation of inelastic shear deformation in realistic models of amorphization of boron carbide is noted, as is a greater reduction in overall strength of polycrystals containing one or a few dominant flaws rather than many diffusely distributed microcracks.

Keywords Continuum mechanics · Geometry · Phase field · Fracture · Twinning · Phase transformation · Finsler space

1 Introduction

When subjected to mechanical stresses exceeding their elastic limit, crystalline materials may undergo one or more of a number of inelastic deformation mechanisms. Such mechanisms include dislocation-mediated plasticity, deformation twinning, stress-induced phase transformations, and various fracture behaviors. Emphasis

Communicated by Andreas Öchsner.

J. D. Clayton (✉)
Impact Physics, US ARL, Aberdeen, MD 21005, USA
E-mail: john.d.clayton1.civ@mail.mil; jdclayt1@umd.edu

J. D. Clayton
A. James Clark School of Engineering, University of Maryland, College Park, MD 20742, USA

J. Knap
Computational and Engineering Sciences, US ARL, Aberdeen, MD 21005, USA

of the present work is on those mechanisms distinct from dislocation plasticity: twinning, solid–solid phase transformations, and fracture in the form of shear failure, cleavage, and/or cavitation. These mechanisms are often encountered in less ductile nonmetals, or in those crystals with structures belonging to space groups of low symmetry, wherein the tendency for dislocation glide is restricted.

The particular material of interest in the present paper, to which a novel and sophisticated constitutive model framework is applied, is boron carbide, with nominal chemical composition B_4C. Boron carbide is a ceramic crystal with rhombohedral (i.e., trigonal) symmetry, and it demonstrates advantages of high elastic stiffness, relatively low mass density, and high hardness. Performance in industrial and engineering applications is hindered by low ductility and a tendency to undergo a stress-induced phase transformation from crystal to glass, often accompanying shear localization and fracture. Experimental evidence for such behavior is reported in [1,2]. Atomic simulation results, obtained either via first principles or molecular dynamics, confirming deformation mechanisms of amorphization and fracture via cavitation or instability include [3–7]. Continuum nonlinear elastic and elastic–plastic models have also been used to predict instability and failure of boron carbide single crystals and polycrystals [8–11]. Deformation twinning has been reported in experiments [12] and atomic simulations [6,7], and twins are also prevalent in certain kinds of boron carbide depending on processing [13].

Various classes of finite deformation continuum physics models have been used to address inelastic deformation mechanisms of present interest. Continuum theories based on the idea of pseudo-slip (similar to continuum crystal plasticity [14,15]) have been invoked to describe deformation twinning [16–18] and cleavage fracture [19–21] in crystals. Continuum damage mechanics models are widely used to describe cavitation and fracture [22,23]. Sharp-interface representations of inelastic mechanisms include cohesive zone models for fracture [24–27] and a level-set model for twinning [28]. Many diffuse-interface representations invoke phase field concepts for modeling fracture [29–32], phase transformations [33–35], and twinning [36–39]. Coupled continuum models of crystal plasticity with phase field representations of fracture also exist [40].

The theory and simulations advanced in the present paper invoke concepts from phase field dynamics and Finsler differential geometry. Regarding the latter, generalized Finsler-geometric continuum mechanics [41–43] incorporates a director vector or a vector of evolving state variables upon which the metric tensor and geometric quantities derived from it (e.g., volume and connection coefficients) depend. Such dependence enables a physically natural and geometrically inspired description of evolving microstructure on the response of the material to mechanical loading. Early work by the present author [44] identified a state vector component of Finsler continuum mechanics with an order parameter of phase field theory. A complete and refined theory was first presented in [41] including solutions to problems involving shear failure and cavitation in magnesium metal. A generalized Finsler-geometric continuum physics framework was developed in [45] that included both additive and multiplicative decompositions of the deformation gradient into elastic and inelastic parts. Solutions for tensile fracture and compressive phase transformations of boron carbide were reported. The variational theory of [41,45] was further focused in [46] to consider spherical inelastic deformation associated with ductile failure or void growth, with solutions developed for ductile tensile failure of magnesium and shear localization in boron carbide. More recently, the theory was extended to consider dynamics and shock wave propagation in [47], including solutions for shock compression of a boron carbide single crystal along its c-axis, wherein inelastic shearing in conjunction with amorphization was permitted on pyramidal planes [7]. In theory and applications reported to date [41,45–47], governing equations are derived via fundamental principles of mathematical physics with material properties obtained from standard experiments or reported results of atomic simulations; thus, few, if any, calibrated material parameters are required.

Developed in this work is the first known continuum model of deformation twinning in boron carbide single crystals. This model incorporates ideas from a prior geometrically nonlinear phase field theory of twinning [36–38]. The present model simultaneously allows for a stress-induced phase change to an amorphous or glassy solid. A single order parameter measures the transition from parent crystal to twinned crystal to glass, as observed for some orientations of single crystals in atomic simulations [7]. Suppression of twinning for other orientations enables transition directly from parent to amorphous phase. Since volume, and thus the material metric, changes with a change in phase (specifically, a mass density increases from crystal to glass [2,34]), the order parameter is assigned as a component of a state vector of generalized pseudo-Finsler space [45]. A second component of this state vector is another order parameter linked to shear softening and cavitation, with a local mass density decreases associated with the latter failure mechanism.

Also reported in this paper are the first known three-dimensional (3-D) finite element (FE) simulations for Finsler-geometric continuum mechanics. Fully resolved polycrystals of polyhedral shape [48–50] are subjected to deformation histories enabling exploration of effects of grain size, shape, and orientation on the mechanical

response of boron carbide. Analytical or simple numerical solutions in prior work [45,46] were restricted to homogeneous deformation of single crystals or stress-free solutions for failed material, while dynamic solutions in [47] were restricted to homogeneous domains behind steady shock fronts. The present, and much more sophisticated, numerical methods enable the potential for understanding and designing polycrystalline boron carbide microstructures for improved failure resistance. Such work at the "mesoscale" complements atomic scale simulations [51,52] whose purpose is virtual design of failure resistant single crystal compositions of boron-based ceramics.

Remaining content is organized as follows. General theory is reviewed in Sect. 2, including geometry, kinematics, and equilibrium and rate equations. The theory is specialized to boron carbide in Sect. 3, allowing for inelastic mechanisms of twinning, amorphization, and failure by shear fracture and cavitation. A basic problem of simple shear of a single crystal of boron carbide is solved in Sect. 4, enabling demonstration of capabilities of the constitutive model and comparison and validation with observations from experiments or atomic simulations reported elsewhere. Implementation of the theory in FE simulations of deforming polycrystals under pure shear or axial compressive loading is reported in Sect. 5. Conclusions follow in Sect. 6.

2 Theory: general concepts

A theory for the mechanical response of deformable solids is presented, consisting of geometric descriptions of reference and spatial configurations and motion between the two. Thermodynamic aspects, balance equations, and kinetics are then described. A multiplicative decomposition of the deformation gradient is invoked, leading to more specific forms of governing equations.

The present discussion is limited to only those theoretical features used in subsequent applications of the paper, and thus justification and elaborate discussion of many aspects of the general theory are often omitted. Such justification and discussion can instead be found in prior work [41,45–47] that comprises a more complete presentation of the Finsler-geometric continuum mechanics theory. A notable simplification to be invoked herein is that the base manifold of each configuration is assigned a Cartesian structure since curvilinear coordinates are not needed for the present applications.

2.1 Geometry and kinematics

Denote by $\mathfrak{M}$ a differentiable manifold of dimension 3 covered by coordinates $\{X^A\}$, and denote an arbitrary material point by $X \in \mathfrak{M}$. To each point is assigned a unique vector $\boldsymbol{D}(X)$ with entries $\{D^A\}$, where $A = 1, 2, 3$. This is referred to here as a director vector or internal state vector, and it need not be a unit vector. Notation $f(X, D)$ implies a dependence of an arbitrary function f on $\{X^A, D^A\}$. The natural or holonomic basis vectors for the generalized Finsler tangent bundle are the fields $\{\frac{\partial}{\partial X^A}, \frac{\partial}{\partial D^A}\}$. The cotangent bundle has the corresponding natural bases $\{dX^A, dD^A\}$. In the present simplified version of the theory, nonlinear connection coefficients N^A_B are prescribed to vanish identically, and there is no need for introduction of non-holonomic basis vectors unlike the more general differential geometric presentations given in [41,45].

The referential metric tensor in this case, which presumes a constant Cartesian basis $\{\frac{\partial}{\partial X^A}\}$ over $\mathfrak{M}$, is

$$\boldsymbol{G}(D) = G_{AB}(D)dX^A \otimes dX^B + G_{AB}(D)dD^A \otimes dD^B. \tag{2.1}$$

Components of this metric are used to raise and lower indices as necessary. Partial differentiation is written

$$\partial_A(\cdot) = \partial(\cdot)/\partial X^A, \qquad \bar{\partial}_A(\cdot) = \partial(\cdot)/\partial D^A. \tag{2.2}$$

The delta derivative $\delta_A(\cdot)$ of Finsler geometry [53] reduces to $\partial_A(\cdot)$ here since nonlinear connection coefficients vanish. Since $\boldsymbol{G}$ does not depend on $\{X^A\}$, Levi–Civita connection coefficients vanish identically, as do horizontal coefficients of the Chern–Rund and Cartan connections. Cartan's tensor has generally nonzero components

$$C^A_{BC} = \tfrac{1}{2}G^{AD}(\bar{\partial}_C G_{BD} + \bar{\partial}_B G_{CD} - \bar{\partial}_D G_{BC}) = G^{AD}C_{BCD}. \tag{2.3}$$

Respective scalar volume elements and volume forms of $\mathfrak{M}$ are [54]

$$\mathrm{d}V = \sqrt{G}\mathrm{d}X^1\mathrm{d}X^2\mathrm{d}X^3, \qquad d\Omega = \sqrt{G}\mathrm{d}X^1 \wedge \mathrm{d}X^2 \wedge \mathrm{d}X^3. \tag{2.4}$$

A differential area form for a compact region of $\mathfrak{M}$ is

$$\Omega = \sqrt{\beta}\mathrm{d}U^1 \wedge \mathrm{d}U^2; \qquad \left[X^A = X^A(U^\alpha),\ (\alpha = 1, 2); \quad \beta^A_\alpha = \frac{\partial X^A}{\partial U^\alpha}, \quad \beta = \det\left(\beta^A_\alpha G_{AB}\beta^B_\beta\right)\right]. \tag{2.5}$$

Let $V^A(X, D)\Omega(X, D)$ be a 2-form, and let V^A be contravariant components of a generic differentiable vector field. For the present case in which the horizontal covariant derivative of G vanishes, Stokes' theorem for generalized pseudo-Finsler geometry is [45,54]

$$\int_{\mathfrak{M}} \left[V^A_{|A} + \left(V^A C^C_{BC} + \bar\partial_B V^A\right) D^B_{;A}\right] d\Omega = \oint_{\partial\mathfrak{M}} V^A N_A \Omega. \tag{2.6}$$

Here, N_A is the unit outward normal to $\partial\mathfrak{M}$, $V^A_{|A}$ is the horizontal covariant derivative of $\boldsymbol{V}$, and $D^B_{;A} = \partial_A D^B + N^B_A$. Motivated by this theorem, a covariant derivative operation $(\cdot)_{||A}$ is defined in a reference coordinate chart as [47]

$$(\cdot)_{||A} = (\cdot)_{|A} + \left[(\cdot)C^C_{BC} + \bar\partial_B(\cdot)\right] D^B_{;A} \qquad \Rightarrow \qquad \int_{\mathfrak{M}} (\cdot)_{||A} d\Omega = \oint_{\partial\mathfrak{M}} (\cdot) N_A \Omega. \tag{2.7}$$

Since herein $N^A_B = 0$ and $\boldsymbol{G}$ does not depend on $\{X^A\}$, the simplifications $V^A_{|A} = \partial_A V^A$ and $D^B_{;A} = \partial_A D^B$ hold.

The description of the spatial configuration manifold $\mathfrak{m}$ and associated geometric quantities exactly parallels that of the reference configuration. Coordinates of points $x \in \mathfrak{m}$ are $\{x^a\}$, and each is assigned a unique vector $\boldsymbol{d}(x)$ with entries $\{d^a\}$. The spatial metric tensor, which presumes a constant Cartesian basis $\{\frac{\partial}{\partial x^a}\}$ over $\mathfrak{m}$, is

$$\boldsymbol{g}(d) = g_{ab}(d)dx^a \otimes dx^b + g_{ab}(d)dd^a \otimes dd^b. \tag{2.8}$$

Partial differentiation is

$$\partial_a(\cdot) = \partial(\cdot)/\partial x^a, \qquad \bar\partial_a(\cdot) = \partial(\cdot)/\partial d^a. \tag{2.9}$$

Since $\boldsymbol{g}$ does not depend on $\{x^a\}$, Levi–Civita connection coefficients and horizontal coefficients of the Chern–Rund and Cartan connections all vanish. Cartan's tensor in the spatial configuration is

$$C^a_{bc} = \tfrac{1}{2}g^{ad}\left(\bar\partial_c g_{bd} + \bar\partial_b g_{cd} - \bar\partial_d g_{bc}\right) = g^{ad}C_{bcd}. \tag{2.10}$$

Volume elements and forms of $\mathfrak{m}$ are

$$\mathrm{d}v = \sqrt{g}\mathrm{d}x^1\mathrm{d}x^2\mathrm{d}x^3, \qquad d\omega = \sqrt{g}\mathrm{d}x^1 \wedge \mathrm{d}x^2 \wedge \mathrm{d}x^3. \tag{2.11}$$

A version of Stokes's theorem like (2.6) applies for $\mathfrak{m}$, as does a definition for differentiation $(\cdot)_{||a}$ analogous to (2.7).

The motion function from $\mathfrak{M}$ to $\mathfrak{m}$ and its inverse at time t are, respectively,

$$x^a(X, t) = \varphi^a(X, t), \qquad X^A(x, t) = \Phi^A(x, t). \tag{2.12}$$

These are a specific case of the more general functions introduced in [46,47] that may include functional dependence on D or d as well. The present simpler definitions are sufficient for applications in this paper. Mappings of state vectors between configurations are the functions

$$d^a(X, D, t) = \theta^a[X, D(X, t), t], \qquad D^A(x, d, t) = \Theta^A[x, d(x, t), t]. \tag{2.13}$$

The deformation gradient and its inverse are, from (2.12) and under the present case of null nonlinear connection coefficients,

$$\boldsymbol{F}(X, t) = F^a_A(X, t)\frac{\partial}{\partial x^a} \otimes dX^A = \partial_A\varphi^a(X, t)\frac{\partial}{\partial x^a} \otimes dX^A, \tag{2.14}$$

$$\boldsymbol{F}^{-1}(x, t) = (F^{-1})^A_a(x, t)\frac{\partial}{\partial X^A} \otimes dx^a = \partial_a\Phi^A(x, t)\frac{\partial}{\partial X^A} \otimes dx^a. \tag{2.15}$$

Determinants of (2.14) and (2.15) are presumed positive. Transformation equations for line elements between configurations are

$$\mathrm{d}x^a = F^a_A \mathrm{d}X^A, \qquad \mathrm{d}X^A = (F^{-1})^A_a \mathrm{d}x^a. \tag{2.16}$$

Transformation equations for volume elements and volume forms are

$$\begin{aligned} \mathrm{d}v = J\mathrm{d}V = \left[\det(F^a_A)\sqrt{g/G}\right]\mathrm{d}V, \quad \mathrm{d}V = J^{-1}\mathrm{d}v = \left[1/\det(F^a_A)\right]\sqrt{G/g}]\mathrm{d}v; \\ d\omega = Jd\Omega, \quad d\Omega = (1/J)d\omega. \end{aligned} \tag{2.17}$$

The symmetric deformation tensor $\boldsymbol{C}$ quantifies the stretch of line elements:

$$\begin{aligned} |\mathrm{d}\boldsymbol{x}|^2 &= F^a_A F^b_B g_{ab} \mathrm{d}X^A \mathrm{d}X^B = C_{AB}\mathrm{d}X^A\mathrm{d}X^B = \langle \mathrm{d}\boldsymbol{X}, \boldsymbol{C}\mathrm{d}\boldsymbol{X}\rangle, \qquad \boldsymbol{C} = C_{AB}dX^A \otimes dX^B \\ &= F^a_A g_{ab} F^b_B dX^A \otimes dX^B. \end{aligned} \tag{2.18}$$

Furthermore, $\det(C^A_B) = \det(C_{AB})/G = J^2$.

Let $D(\cdot)/Dt$ denote the material time derivative, which is defined here as the partial time derivative of a quantity at a fixed material point X and at fixed internal state D. The material velocity (vector) is defined as the material time derivative of position:

$$\boldsymbol{v}(X,t) = \frac{\partial \boldsymbol{x}(X,t)}{\partial t} = \frac{\partial \varphi^a(X,t)}{\partial t}\frac{\partial}{\partial x^a}, \qquad v^a = \frac{Dx^a}{Dt}. \tag{2.19}$$

When there is no chance of confusion, a superposed dot is also used for material time differentiation. A special case is the time derivative of internal state, which is a partial derivative at constant X [47]:

$$\dot{\boldsymbol{D}}(X,t) = \frac{\partial D^A(X,t)}{\partial t}\frac{\partial}{\partial D^A}. \tag{2.20}$$

2.2 Governing equations

In this work, quasi-static conditions for mechanical momentum are assumed, but dynamic evolution of the state vector field (i.e., order parameter kinetics) is enabled. Isothermal conditions are also presumed. Such simplifications are common in phase field applications [33]. Governing equations for the fully dynamic case—including material inertia and temperature and entropy changes—are derived in [47].

Referential mass density ρ_0 is related to spatial mass density ρ via application of (2.17):

$$\rho_0 = \rho J. \tag{2.21}$$

Denote by $n_a \mathrm{d}a$ and $N_A \mathrm{d}A$ area elements on the boundaries of $\mathfrak{m}$ and $\mathfrak{M}$, related by the usual Nanson's formula [55] at $x = x(X,t)$:

$$N_A \mathrm{d}A = J^{-1} F^a_A n_a \mathrm{d}a. \tag{2.22}$$

Letting $\mathrm{d}P^a = t^a \mathrm{d}a = t^a_0 \mathrm{d}A$ be a component of a differential mechanical force vector, traction components are

$$t^a = \sigma^{ab} n_b, \qquad t^a_0 = g^{ab} P^A_b N_A. \tag{2.23}$$

The first Piola–Kirchhoff stress P^A_a and symmetric Cauchy stress σ^{ab} are related by the deformation gradient and Jacobian determinant as [41,45–47]

$$\sigma^{ab} = J^{-1} g^{ac} P^A_c F^b_A = \sigma^{ba}. \tag{2.24}$$

Using Stokes' theorem (2.6) for Finsler space, the following local balance of linear momentum can be derived for the quasi-static case [47], wherein body forces and acceleration $D\boldsymbol{v}/Dt$ are presumed null:

$$P^A_{a||A} = \partial_A P^A_a + \left(P^A_a C^C_{BC} + \bar{\partial}_B P^A_a\right)\partial_A D^B = 0. \tag{2.25}$$

The differential notation $(\cdot)_{||A}$ is introduced in (2.7).

Free energy density per unit reference volume on $\mathfrak{M}$ is of the following general form for isothermal conditions:

$$\psi = \psi\,(\boldsymbol{F}, \boldsymbol{D}, \nabla\boldsymbol{D}, \boldsymbol{G}) = \psi(F^a_A, D^A, \partial_B D^A, G_{AB}), \tag{2.26}$$

recalling a Cartesian reference basis with vanishing nonlinear connection is imposed such that the horizontal material gradient $\nabla(\cdot)$ is equivalent to the partial derivative with respect to reference coordinates $\{X^a\}$. The internal state vector $\boldsymbol{D}$ is interpreted as a vector-valued set of order parameter(s). Thermodynamic forces are obtained via the material time derivative and chain rule applied to (2.26):

$$\dot{\psi} = \frac{\partial\psi}{\partial F^a_A}\dot{F}^a_A + \frac{\partial\psi}{\partial D^A}\dot{D}^A + \frac{\partial\psi}{\partial\left(\partial_B D^A\right)}\frac{\mathrm{D}}{\mathrm{D}t}\left(\partial_B D^A\right) + \frac{\partial\psi}{\partial G_{AB}}\dot{G}_{AB} = P^A_a\dot{F}^a_A + Q_A\dot{D}^A + Z^B_A\frac{\mathrm{D}}{\mathrm{D}t}\left(\partial_B D^A\right) + S^{AB}\dot{G}_{AB}. \tag{2.27}$$

Spatial coordinate invariance requires [41]

$$\psi = \psi[\boldsymbol{C}(\boldsymbol{F}, \boldsymbol{g}), \boldsymbol{D}, \nabla\boldsymbol{D}, \boldsymbol{G}] = \psi(C_{AB}, D^A, \partial_B D^A, G_{AB}). \tag{2.28}$$

In prior work [41], a local equilibrium equation was derived for micromomentum, containing terms in $\boldsymbol{Q}$ and $\boldsymbol{Z}$. In the dynamic regime, the kinetic equation for internal state vector components D^A is found by setting the residual of that equilibrium equation proportional to the negative rate of internal state as declared in [47]

$$\dot{D}^K = -\mathsf{L}^{KC}[Q_C - \partial_A Z^A_C - \bar{\partial}_B Z^A_C\partial_A D^B - Z^B_C C^D_{ED}\partial_B D^E + (S^{AB} + \psi G^{AB})\bar{\partial}_C G_{AB}]. \tag{2.29}$$

Here, L^{KC} is a positive definite matrix of material constants dictating the time scale for kinetics. Equation (2.29) suggests that order parameter(s) evolve in time so that at equilibrium, the term in square braces vanishes in accordance with the static director momentum equation in [41]. Equation (2.29) can be expressed in condensed form as

$$\dot{D}^K = -\mathsf{L}^{KC}\left[\frac{\partial\psi}{\partial D^C} - \nabla_A\left(\frac{\partial\psi}{\partial(\partial_A D^C)}\right) + \cdots\right] = -\mathsf{L}^{KC}\frac{\delta\psi}{\delta D^C}, \tag{2.30}$$

where terms are truncated only for presentation purposes and the notation $\delta\psi/\delta\boldsymbol{D}$ here denotes the thermodynamic derivative typical in phase field theory, not to be confused with the delta derivative of Finsler geometry. This equation is the generalized Finsler analog to the time-dependent Ginzburg–Landau or Allen–Cahn equations of phase field kinetics [35,56,57].

Thorough consideration of the First and Second Laws of Thermodynamics requires introduction of fundamental postulates for energy conservation and entropy production as well as distinct definitions of thermodynamic quantities such internal energy, Helmholtz free energy, temperature, entropy, and heat flux. Partial progress in this regard is reported in [47], where it is emphasized that special care must be taken for definitions of kinematic rates, energy rates, and Reynolds' transport theorem in generalized Finsler space. In that work, the First Law is addressed for the adiabatic case. Herein, where isothermal conditions apply, a scalar dissipation function D can be introduced similarly to that in [33,57], which, when kinetic equation (2.30) is invoked, is always nonnegative:

$$\mathsf{D} = \mathsf{F}_K\dot{D}^K = \mathsf{L}^{KC}\frac{\delta\psi}{\delta D^K}\frac{\delta\psi}{\delta D^C} \geq 0. \tag{2.31}$$

The conjugate thermodynamic force component is $\mathsf{F}_K = -\delta\psi/\delta D^K$. Thus, (2.31) is essentially in accord with an irreversibility principle. A more formal treatment of thermodynamics remains to be pursued in future work.

2.3 Multiplicative descriptions

As in prior work [45,46], a multiplicative decomposition of deformation gradient $\boldsymbol{F}$ of (2.14) is used:

$$\boldsymbol{F} = \boldsymbol{F}^E\boldsymbol{F}^D, \qquad F^a_A = (F^E)^a_\alpha(F^D)^\alpha_A. \tag{2.32}$$

The elastic or mechanically recoverable deformation, $\boldsymbol{F}^E$, and the residual/inelastic deformation due to changes in internal state, $\boldsymbol{F}^D$, both must have positive determinants. The functional forms of these two-point tensors are [45,46]

$$(F^E)^a_\alpha = (F^E)^a_\alpha(X, t), \qquad (F^D)^\alpha_A = (F^D)^\alpha_A[D(X, t)]. \tag{2.33}$$

Greek indices correspond to potentially anholonomic space [55,58] of the intermediate configuration. Multiplicative decompositions of the referential Sasaki metric tensor and its inverse are

$$G_{AB}(D) = \delta_{AB} B(D), \qquad G^{AB}(D) = \delta^{AB} B^{-1}(D). \tag{2.34}$$

noting that the dependence on internal state is relegated to a positive scalar function $B(D)$ that scales the Cartesian metric δ_{AB}. Such a form is consistent with the use of Cartesian basis vectors $\{\frac{\partial}{\partial X^A}\}$ throughout this paper. Analogously for the spatial metric,

$$g_{ab}(d) = \delta_{ab} b(d), \qquad g^{ab}(d) = \delta^{ab} b^{-1}(d), \tag{2.35}$$

with scalar function $b(d) > 0$. The metric tensor for the intermediate configuration [59] is

$$g_{\alpha\beta}(D) = \delta_{\alpha\beta} B(D), \qquad g^{\alpha\beta}(D) = \delta^{\alpha\beta} B^{-1}(D). \tag{2.36}$$

Determinants of metrics are

$$G(D) = B^3(D), \quad g(d) = b^3(d); \qquad \tilde{g}(D) = \det[g_{\alpha\beta}(D)] = B^3(D). \tag{2.37}$$

Volume element $\mathrm{d}\tilde{v}$ and volume form $d\tilde{\omega}$ on the intermediate space are

$$\begin{aligned} &\mathrm{d}\tilde{v} = \{\det[(F^D)^a_A]\sqrt{\tilde{g}/G}\}\mathrm{d}V = J^D \mathrm{d}V, \quad \mathrm{d}\tilde{v} = \{\det[(F^{E-1})^\alpha_a]\sqrt{\tilde{g}/g}\}\mathrm{d}v = (J^E)^{-1}\mathrm{d}v; \\ &d\tilde{\omega} = J^D d\Omega = (J^E)^{-1} d\omega. \end{aligned} \tag{2.38}$$

Jacobian determinants for inelastic and elastic mappings are respectively defined as

$$J^D = \det[(F^D)^a_A]\sqrt{\tilde{g}/G} = \det\left[(F^D)^a_A\right], \qquad J^E = \det\left[(F^E)^a_\alpha\right]\sqrt{g/\tilde{g}} = \det\left[(F^E)^a_\alpha\right](b/B)^{3/2}. \tag{2.39}$$

Further explanation of the use of Weyl scaling [60] in the conformal transformation of the Cartesian metrics in (2.34), (2.35), and (2.36) can be found in [41,46,47].

As in prior treatments [45,46] the free energy ψ of (2.26) is split into a sum of elastic strain energy density W and structure/internal state-dependent energy density f:

$$\psi(F^a_A, D^A, \partial_B D^A) = W[(F^E)^a_\alpha, D^A] + f(D^A, \partial_B D^A). \tag{2.40}$$

Dependence on the metric tensor $\boldsymbol{G}$ is not needed upon consideration of (2.34) since dependence on $\boldsymbol{D}$ is already included in the list of arguments. Importantly, the general dependence of energy density on $\boldsymbol{F}$ in (2.26) is replaced by a dependence on elastic part $\boldsymbol{F}^E$. Applying (2.40), thermodynamic forces of (2.27) become

$$\begin{aligned} P^A_a &= \frac{\partial\psi}{\partial F^a_A} = \frac{\partial W}{\partial F^a_A} = (F^{D\,-1})^A_\alpha \frac{\partial W}{\partial (F^E)^a_\alpha}; \\ Q_A &= \frac{\partial\psi}{\partial D^A} = \frac{\partial W}{\partial D^A} + \frac{\partial f}{\partial D^A} - P^B_a (F^E)^a_\alpha \frac{\partial (F^D)^\alpha_B}{\partial D^A}, \qquad Z^B_A = \frac{\partial\psi}{\partial(\partial_B D^A)} = \frac{\partial f}{\partial(\partial_B D^A)}. \end{aligned} \tag{2.41}$$

Spatial invariance like (2.28) suggests W should depend on symmetric tensor $\boldsymbol{C}^E$ rather than $\boldsymbol{F}^E$, with

$$(C^E)_{\alpha\beta} = (F^E)^a_\alpha \delta_{ab} (F^E)^b_\beta = (F^{D\,-1})^A_\alpha \bar{C}_{AB} (F^{D\,-1})^B_\beta, \qquad \bar{C}_{AB} = F^a_A \delta_{ab} F^b_B = b^{-1} C_{AB}. \tag{2.42}$$

3 Theory: twinning, phase change, and fracture

The general theory of Sect. 2 is now specialized to address inelastic deformation mechanisms of twinning, solid–solid phase transformations, and fracture. The model material is the ceramic crystal boron carbide, wherein the specific phase change in study is stress-induced amorphization, and wherein fracture mechanisms of study are simultaneous shear softening and cavitation.

3.1 Geometry and kinematics

Considered here is a crystalline material element with a single potentially active twin system and a single cleavage plane coincident with the habit plane of twinning. The internal state vector field $\boldsymbol{D}$ referred to reference coordinates consists of two nonzero entries in a preferred Cartesian basis, where $\{\frac{\partial}{\partial X^1}\}$ is normal to the fracture/habit plane, and where $\{\frac{\partial}{\partial X^2}\}$ is aligned parallel to the direction of twinning shear. Basis vector $\{\frac{\partial}{\partial X^3}\}$ also lies in the fracture/habit plane, with a direction orthogonal to the direction of twinning shear. Unit basis vectors $\{\frac{\partial}{\partial D^1}, \frac{\partial}{\partial D^2}, \frac{\partial}{\partial D^3}\}$ are of the same orientation as their Cartesian (X) counterparts. Specifically in this coordinate system, the column vector of internal state variables is defined as

$$\boldsymbol{D}(X,t) = \begin{bmatrix} D^1(X,t) \\ D^2(X,t) \\ D^3(X,t) \end{bmatrix} = l \begin{bmatrix} \xi(X,t) \\ \eta(X,t) \\ 0 \end{bmatrix}. \tag{3.1}$$

Order parameters ξ and η are dimensionless fields at least twice differentiable with respect to X^A and once with respect to t, and l is a constant regularization length. Physically, D^1 corresponds to crack opening, crack sliding, and/or cavitation on a plane with orientation (unit normal vector) $\boldsymbol{M}$ parallel to $\{\frac{\partial}{\partial X^1}\}$ and $\{\frac{\partial}{\partial D^1}\}$. Physically, D^2 corresponds to microdisplacement in the direction associated with twinning shear, $\boldsymbol{S}$, which is a unit vector parallel to $\{\frac{\partial}{\partial X^2}\}$ and $\{\frac{\partial}{\partial D^2}\}$. Variable D^2 is also conveniently used to denote a possible transformation from crystal to glassy phase corresponding to a plane with the same unit normal $\boldsymbol{M}$. Later, ξ will be mathematically related to dilatation kinematics and elastic stiffness degradation, and η will be related to the shearing-type deformation gradient contribution(s) from twinning and/or amorphization.

Specifically, $\xi \in [0, 1]$, where

$$\begin{aligned} &\xi(X,t) = 0 \forall X \in \text{ undamaged material at time } t, \\ &\xi(X,t) \in (0,1) \forall X \in \text{partially degraded material at time } t, \\ &\xi(X,t) = 1 \forall X \in \text{ fully failed material at time } t. \end{aligned} \tag{3.2}$$

Also, let $\eta_0 \in (0, 1]$ be a constant for a particular material system. Then $\eta \in [0, 1]$, where

$$\begin{aligned} &\eta(X,t) = 0 \forall X \in \text{ parent crystal at time } t, \\ &\eta(X,t) \in (0,\eta_0) \forall X \in \text{ twin boundary zone at time } t, \\ &\eta(X,t) \in (0,1) \forall X \in \text{ phase boundary zone at time } t, \\ &\eta(X,t) \geq \eta_0 \forall X \in \text{ fully twinned material at time } t, \\ &\eta(X,t) = 1 \forall X \in \text{ fully amorphous material at time } t. \end{aligned} \tag{3.3}$$

The physical rationale for (3.3) with $\eta_0 < 1$ follows atomic simulation results [7] that demonstrate amorphization subsequent to twinning, i.e., favorable phase transitions within twinned regions. It will be demonstrated later how the model can be reduced to allow η to represent either twinning or amorphization rather than both simultaneously, behaviors that depend upon the particular crystallographic deformation system of interest [6,7]. Regardless, $\eta > 0$ is used to account for inelastic shearing and densification, where the former is attributed to some combination of twinning dislocations and localized slip in amorphous bands and the latter is attributed to a reduction in free volume in transformation zones.

The spatial versions of dimensionless state variables, denoted by $\hat{\xi}(x,t)$ and $\hat{\eta}(x,t)$, follow the simple canonical transformation rules used in prior work [41,45]:

$$\begin{aligned} &\xi = \hat{\xi} \circ \varphi \Leftrightarrow \xi(X,t) = \hat{\xi}[\varphi(X,t),t] \Leftrightarrow d^1(x,t) = \hat{\xi}(x,t)l = D^1[X(x,t),t], \\ &\eta = \hat{\eta} \circ \varphi \Leftrightarrow \eta(X,t) = \hat{\eta}[\varphi(X,t),t] \Leftrightarrow d^2(x,t) = \hat{\eta}(x,t)l = D^2[X(x,t),t]. \end{aligned} \tag{3.4}$$

Recall that φ is the motion of (2.12). The same fixed regularization length l is used in the spatial configuration. Other more complex transformations between configurations are not considered since they would lack any apparent physical justification. On the other hand, vectors $\boldsymbol{D}$ and $\boldsymbol{d}$ follow the usual transformation formulae of (pseudo)-Finsler geometry [41,53] for changes of coordinates at fixed configuration.

The material and spatial metric tensors in (2.34) and (2.35) are assigned Weyl-type scaling behavior [41,46,60]:

$$B(\xi,\eta)=\exp\left[\tfrac{1}{3}(m\xi^2+k\eta^2)\right],\qquad b(\hat{\xi},\hat{\eta})=\exp\left[\tfrac{1}{3}(m\hat{\xi}^2+k\hat{\eta}^2)\right]. \tag{3.5}$$

Here, m and k are scalar constants quantifying the magnitude of volume change associated with fracture and amorphization, respectively. Fracture by cavitation leads to dilatation, corresponding to $m>0$, while amorphization in boron carbide is associated with densification, implying $k<0$. From (3.4) and (3.5), the ratio of determinants of metric tensors is unity:

$$g[x(X,t),t]/G(X,t)=b^3[x(X,t),t]/B^3(X,t)=1\Rightarrow J=\det\left(F^a_A\right)\sqrt{g/G}=\det\left(F^a_A\right). \tag{3.6}$$

Components of Cartan's tensors in (2.3) and (2.10) are functions of (ξ,η) and $(\hat{\xi},\hat{\eta})$, respectively. Specifically needed in momentum balance (2.25) and kinetic law (2.29) are three traces of referential Cartan tensor C^A_{BC}:

$$C^A_{1A}=(\tfrac{3}{2}\bar{\partial}_1 B)/B=m\xi/l,\qquad C^A_{2A}=(\tfrac{3}{2}\bar{\partial}_2 B)/B=k\eta/l,\qquad C^A_{3A}=0. \tag{3.7}$$

Contributions from changes in internal state to the deformation gradient are embedded in the two-point tensor $\boldsymbol{F}^D(\boldsymbol{D})=\boldsymbol{F}^D(\xi,\eta)$ introduced in (2.32). First consider the contribution from cavitation, which is treated as isotropic [34,46]. Specifically, define

$$\boldsymbol{F}^\xi(\xi)=[1+x_\xi\phi_\xi(\xi)]\mathbf{1},\qquad \phi_\xi(\xi)=\alpha\xi^2+2(2-\alpha)\xi^3+(\alpha-3)\xi^4. \tag{3.8}$$

Constant x_ξ is positive for expansion. Polynomial $\phi_\xi:[0,1]\to[0,1]$ is an interpolation function obeying $\phi'_\xi(0)=\phi'_\xi(1)=0$, and $\alpha\in[0,6]$ is a constant [33,36]. Next consider the contribution from a change in phase (crystal to glass), which is here presumed to coincide with uniaxial straining normal to the basal plane [2,45]. Let

$$\bar{\boldsymbol{F}}^\eta(\eta)=\mathbf{1}+x_\eta\phi_\eta(\eta)\boldsymbol{M}\otimes\boldsymbol{M},\qquad \phi_\eta(\eta)=\beta\eta^2+2(2-\beta)\eta^3+(\beta-3)\eta^4. \tag{3.9}$$

Constant x_η is negative for densification. Polynomial $\phi_\eta:[0,1]\to[0,1]$ obeys $\phi'_\eta(0)=\phi'_\eta(1)=0$, and $\beta\in[0,6]$ is a constant. Finally, consider the contribution from deformation twinning and inelastic shear. As in [36,37], twinning on a single system with unit plane normal $\boldsymbol{M}$ and orthogonal shearing direction $\boldsymbol{S}$ is the isochoric simple shear

$$\boldsymbol{F}^\eta_0(\eta)=\mathbf{1}+\gamma_0\phi_0(\eta)\boldsymbol{S}\otimes\boldsymbol{M},\qquad \phi_0(\eta)=\chi\eta^2+2(2-\chi)\eta^3+(\chi-3)\eta^4. \tag{3.10}$$

The maximum magnitude of twinning shear (and/or possible shearing accommodated by localization in transformation zones) is the constant γ_0, and $\phi_0(\eta)$ is an interpolation function with constant $\chi\in[0,6]$. The total deformation gradient contribution from changes of internal state is the product of the deformation tensors in the first of each of (3.8), (3.9), and (3.10):

$$\boldsymbol{F}^D(\xi,\eta)=\boldsymbol{F}^\xi(\xi)\bar{\boldsymbol{F}}^\eta(\eta)\boldsymbol{F}^\eta_0(\eta). \tag{3.11}$$

The total inelastic volume change, consulting (2.39), becomes

$$J^D(\xi,\eta)=[1+x_\xi\phi_\xi(\xi)]^3[1+x_\eta\phi_\eta(\eta)]. \tag{3.12}$$

See also [61–63] for finite deformation theories containing a multiplicative decomposition of inelastic deformations representing various lattice defects and structural transformation mechanisms.

Consider a fully cavitated material element at X with $\xi(X)=1$, but with $\eta(X)=0$. Consistency of (3.5) and (3.12) leads to the following relationship between constants m and x_ξ: $\sqrt{G}=\exp(m/2)=J^D(1,0)=(1+x_\xi)^3$. Analogously, consideration of a fully transformed but undamaged material element furnishes a relationship between k and x_η: $\sqrt{G}=\exp(k/2)=J^D(0,1)=1+x_\eta$. The selection process for m, k, l, and remaining independent constants α, β, χ, γ_0, and η_0 particular to boron carbide will be discussed later in Sect. 3.5.

3.2 Energy function and thermodynamic forces

Thermodynamics of Sect. 2.3 is now revisited in consideration of the more detailed geometry and kinematics in Sect. 3.1. Let $\nabla(\cdot)$ denote covariant differentiation with respect to $\boldsymbol{X}$. Recalling $\boldsymbol{D}(\xi,\eta)=[\xi l,\eta l,0]^{\mathrm{T}}$ in the present special Cartesian frame and with $\boldsymbol{C}^E$ defined in (2.42), the free energy function of (2.40) is refined as follows:

$$\begin{aligned}\psi(\boldsymbol{F},\boldsymbol{D},\nabla\boldsymbol{D}) &= W(\boldsymbol{F}^E,\xi)+f(\xi,\eta,\nabla\xi,\nabla\eta)\\ &= W(\boldsymbol{C}^E,\xi)+f_\xi(\xi)+f_\eta(\eta)+\boldsymbol{\zeta}:\nabla\xi\otimes\nabla\xi+\boldsymbol{\kappa}:\nabla\eta\otimes\nabla\eta.\end{aligned}\tag{3.13}$$

The strain energy function used here is a nonlinear elastic, compressible neo-Hookean model [37,41,50], modified to account for degradation of the shear modulus with cumulative damage ($\xi>1$):

$$W=\tfrac{1}{2}K\left(\ln J^E\right)^2+\tfrac{1}{2}(1-\xi)^2\mu\left[\mathrm{tr}\boldsymbol{C}^E-3-2\ln J^E\left(1+\tfrac{1}{3}\ln J^E\right)\right],\tag{3.14}$$

where from (2.39), (2.42), and (3.5), it follows that $J^E=\sqrt{\det\boldsymbol{C}^E}$. The bulk modulus is K, and the initial shear modulus is μ. The factor of $(1-\xi)^2$ accounts for reduction in the latter due to fracture. The bulk modulus can be assigned a more sophisticated form in which degradation occurs in tension but not in compression, as in [31,50], an approach that will be invoked later in Sect. 5. A slightly different compressible neo-Hookean elastic potential is used in the phase field fracture model of [32]. Denoting the surface energy of fracture by Υ, the standard quadratic form of phase field fracture models [31,64] is invoked for $f_\xi(\xi)$:

$$f_\xi=(\Upsilon/l)\xi^2.\tag{3.15}$$

The potential $f_\eta(\eta)$ is the sum of a quadratic form for amorphization and a double-well for twinning:

$$f_\eta=\hat{A}\eta^2+12(\Gamma/l)\eta^2(\eta_0-\eta)^2\mathrm{H}(\eta_0-\eta).\tag{3.16}$$

Here, $\hat{A}$ is related to the energy barrier for solid–solid phase transformation from crystal to glass [34], Γ is the twin/phase boundary surface energy, and $\mathrm{H}(\cdot)$ is the Heaviside function. The latter ensures that the energy of a twinned domain vanishes for $\eta\geq\eta_0$, in agreement with (3.3). The coefficients in the gradient contributions are defined as [50]

$$\boldsymbol{\zeta}=\Upsilon l[\mathbf{1}+\vartheta_\xi(\mathbf{1}-\boldsymbol{M}\otimes\boldsymbol{M})],\qquad \boldsymbol{\kappa}=\tfrac{3}{4}\Gamma l[\mathbf{1}+\vartheta_\eta(\mathbf{1}-\boldsymbol{M}\otimes\boldsymbol{M})].\tag{3.17}$$

Scalars ϑ_ξ and ϑ_η penalize fracture and twinning, respectively, on planes of orientations other than $\boldsymbol{M}$. For isotropic free surface energy, $\vartheta_\xi=0$, and for isotropic twin/phase boundary energy, $\vartheta_\eta=0$. The above representation of anisotropic surface energies is similar to that of [39], but others are possible [65].

Invoking (3.13)–(3.17), thermodynamic forces of (2.41) are computed as follows:

$$P_a^A=(1-\xi)^2\mu[(F^E)_a^\alpha(F^{D-1})_\alpha^A-(1+\tfrac{2}{3}\ln J^E)(F^{-1})_a^A]+K\ln J^E(F^{-1})_a^A;\tag{3.18}$$

$$\begin{aligned}Q_1&=\frac{1}{l}\frac{\partial\psi}{\partial\xi}=\frac{1}{l}\left[\frac{\partial W}{\partial\xi}+\frac{\partial f_\xi}{\partial\xi}-P_a^B(F^E)_\alpha^a\frac{\partial(F^D)_B^\alpha}{\partial\xi}\right],\\ Q_2&=\frac{1}{l}\frac{\partial\psi}{\partial\eta}=\frac{1}{l}\left[\frac{\partial f_\eta}{\partial\eta}-P_a^B(F^E)_\alpha^a\frac{\partial(F^D)_B^\alpha}{\partial\eta}\right];\end{aligned}\tag{3.19}$$

$$\begin{aligned}Z_1^B&=\frac{1}{l}\frac{\partial\psi}{\partial(\partial_B\xi)}=2\Upsilon\left[\delta^{AB}+\vartheta_\xi(\delta^{AB}-M^AM^B)\right]\partial_A\xi,\\ Z_2^B&=\frac{1}{l}\frac{\partial\psi}{\partial(\partial_B\eta)}=\tfrac{3}{2}\Gamma\left[\delta^{AB}+\vartheta_\eta(\delta^{AB}-M^AM^B)\right]\partial_A\eta.\end{aligned}\tag{3.20}$$

Consideration of the steps involved in transformation of the arguments of free energy functions in (2.26), (2.28), (2.40), and (3.13) proves instructive. In this regard, the condensed notation $\psi(\boldsymbol{F};\boldsymbol{D},\nabla\boldsymbol{D},\boldsymbol{G})=\psi(\boldsymbol{F};\cdot)$ is used, noting that the terms $(\cdot)=(\boldsymbol{D},\nabla\boldsymbol{D},\boldsymbol{G})$ are all defined with respect to the reference configuration and thus are invariant under transformations of the spatial frame. The transformation $\psi(\boldsymbol{F};\cdot)\rightarrow\psi(\boldsymbol{C};\cdot)$ from (2.26) to (2.28) is standard in continuum mechanics and ensures objectivity since $\boldsymbol{C}=\boldsymbol{F}^{\mathrm{T}}\boldsymbol{F}$ is referred

completely to reference coordinates. The form in (2.40) can be obtained from (2.26) using (2.32), i.e., $\boldsymbol{F}^E(\boldsymbol{F},\boldsymbol{D}) = \boldsymbol{F}\cdot(\boldsymbol{F}^D)^{-1}(\boldsymbol{D})$ enables $\psi(\boldsymbol{F};\cdot)\to\psi(\boldsymbol{F}^E;\cdot)$. Objectivity is then enabled in (3.13) by replacing argument $\boldsymbol{F}^E$ with $\boldsymbol{C}^E$, i.e., $\psi(\boldsymbol{F}^E;\cdot)\to\psi(\boldsymbol{C}^E;\cdot)$. This follows from kinematic definition (2.42) which can be manipulated to give $\boldsymbol{C}^E$ in terms of $\boldsymbol{C}$ and $\boldsymbol{D}$ as $\boldsymbol{C}^E = b\cdot(\boldsymbol{F}^D)^{-1}\boldsymbol{C}(\boldsymbol{F}^D)^{-1}$, where the Weyl scaling factor and inverse inelastic deformation are of the respective forms $b = b(\boldsymbol{D})$ and $(\boldsymbol{F}^D)^{-1} = (\boldsymbol{F}^D)^{-1}(\boldsymbol{D})$.

3.3 Governing equations

The balance laws and kinetic relations of Sect. 2.2 are specialized as follows for the geometry, kinematics, and thermodynamics pertaining to the present application (e.g., boron carbide). First, linear momentum balance (2.25) reduces to

$$d_A P_a^A + P_a^A C_{BC}^C \partial_A D^B = 0. \tag{3.21}$$

The following notation is used:

$$\frac{d}{dX^A}[(\cdot)(X,D,t)] = \frac{\partial}{\partial X^A}[(\cdot)(X,D,t)] + \frac{\partial}{\partial D^B}[(\cdot)(X,D,t)]\frac{\partial D^B(X,t)}{\partial X^A} \Rightarrow d_A(\cdot) = \partial_A(\cdot) + \bar{\partial}_B(\cdot)\partial_A D^B. \tag{3.22}$$

In the present preferred Cartesian coordinate system, the three distinct equations in (3.21) are, with (3.7),

$$d_A P_a^A + P_a^A(m\xi\partial_A\xi + k\eta\partial_A\eta) = 0. \tag{3.23}$$

The kinetic equations for the internal state vector (i.e., order paramters) in (2.29) become, invoking the simplification of diagonal kinetic coefficient matrix L^{KC},

$$\begin{aligned}\dot{\xi} &= -(\mathsf{L}_\xi l^2/\Upsilon)\left[Q_1 - d_A Z_1^A - Z_1^A(m\xi\partial_A\xi + k\eta\partial_A\eta) + 2m\xi\psi/l\right],\\ \dot{\eta} &= -(\mathsf{L}_\eta l^2/\Gamma)\left[Q_2 - d_A Z_2^A - Z_2^A(m\xi\partial_A\xi + k\eta\partial_A\eta) + 2k\eta\psi/l\right].\end{aligned} \tag{3.24}$$

Positive kinetic coefficients with dimensions of 1/time are the two constants L_ξ and L_η. In some problems considered later, energy minimization is used to directly obtain equilibrium states in lieu of time integration of one or both kinetic equations in (3.24). In such cases, fields $\boldsymbol{\varphi}(X)$, $\xi(X)$, and/or $\eta(X)$ are sought at particular time t satisfying the conditions

$$\begin{aligned}\min_{\boldsymbol{\varphi},\boldsymbol{D}}[\Psi(\boldsymbol{\varphi},\boldsymbol{D})] &= \min_{x,\xi,\eta}\left[\int_{\mathfrak{M}}\psi[F_A^a(X,t),\xi(X,t),\eta(X,t),\partial_A\xi(X,t),\partial_A\eta(X,t)]\mathrm{d}\Omega\right]\\ &= \min_{x,\xi,\eta}\left[\int_{\mathfrak{M}}\bar{\psi}[F_A^a(X,t),\xi(X,t),\eta(X,t),\partial_A\xi(X,t),\partial_A\eta(X,t)]\mathrm{d}\Omega_0\right]\end{aligned} \tag{3.25}$$

subject to any constraints imposed by essential boundary conditions on $\boldsymbol{D}$ along $\partial\mathfrak{M}$. In the final expression, $\bar{\psi} = \psi\sqrt{G}$ is the appropriately scaled free energy density, and Ω_0 is the original volume of the domain prior to any changes of internal state affecting the determinant G of the pseudo-Finsler metric tensor. For example, in the context of FE simulations of Sect. 5, Ω_0 represents the initial FE mesh in Cartesian space.

3.4 Linearization

A version of the theory with linearized kinematics is invoked in some numerical simulations reported later. In such a setting, the distinction between spatial and referential configurations is not made explicit, and thus a single set of coordinates $\{X^A, D^A\}$ with $A = 1,2,3$ suffices. The referential generalized pseudo-Finsler metric tensor $\boldsymbol{G}(\boldsymbol{D})$ is of the same form as in (2.1), (2.34), and (3.5), and Cartan's tensor thus still obeys (3.7). The same Cartesian system of basis vectors and the same set of order parameters (ξ,η) from Sect. 3.1 are invoked for this partially linearized theory, which does feature nonlinear material behavior for non-trivial cases wherein order parameters do not vanish.

Linearized kinematics are similar to those employed in prior phase field theory [36–38]. Denote the displacement field by $\boldsymbol{u} = \boldsymbol{u}(X, t)$. Let $\nabla(\cdot)$ denote the covariant derivative with respect to $\boldsymbol{X}$. The displacement gradient is decomposed into elastic and state-dependent parts as follows:

$$\nabla \boldsymbol{u}(X, t) = \boldsymbol{\beta}^E(X, t) + \boldsymbol{\beta}^D[\boldsymbol{D}(X, t)]. \tag{3.26}$$

The elastic distortion is $\boldsymbol{\beta}^E(X, t)$ and is related to the elastic deformation gradient of (2.32) via linearization according to the approximation $\boldsymbol{\beta}^E \approx \boldsymbol{F}^E - \boldsymbol{1}$. If the internal state and total distortion $\nabla \boldsymbol{u}$ are known, then $\boldsymbol{\beta}^E$ can be obtained from inversion of (3.26), i.e., $\boldsymbol{\beta}^E(\nabla \boldsymbol{u}, \boldsymbol{D}) = \nabla \boldsymbol{u} - \boldsymbol{\beta}^D(\boldsymbol{D})$. The state-dependent contribution is further specified as

$$\boldsymbol{\beta}^D(\xi, \eta) = x_\xi \phi_\xi(\xi)\boldsymbol{1} + x_\eta \phi_\eta(\eta)\boldsymbol{M} \otimes \boldsymbol{M} + \gamma_0 \phi_0(\eta)\boldsymbol{S} \otimes \boldsymbol{M}, \tag{3.27}$$

where the first term accounts for dilatation from cavitation, the second accounts for densification from amorphization, and the third accounts for shearing from twinning. Notation for particular quantities in each term is consistent with that of Sect. 3.1. Denote the total strain tensor $\boldsymbol{\epsilon}$ and the elastic strain tensor $\boldsymbol{\epsilon}^E$ as, respectively,

$$\boldsymbol{\epsilon} = \tfrac{1}{2}[\nabla \boldsymbol{u} + (\nabla \boldsymbol{u})^{\mathrm{T}}], \qquad \boldsymbol{\epsilon}^E = \tfrac{1}{2}[\boldsymbol{\beta}^E + (\boldsymbol{\beta}^E)^{\mathrm{T}}]. \tag{3.28}$$

Definitions in (3.26)–(3.28) imply existence of the functional form $\boldsymbol{\epsilon}^E = \boldsymbol{\epsilon}^E(\nabla \boldsymbol{u}, \xi, \eta)$.

For the linearized theory, the free energy density of (2.26) and (3.13) is replaced with

$$\begin{aligned} \psi(\nabla \boldsymbol{u}, \boldsymbol{D}, \nabla \boldsymbol{D}) &= W(\boldsymbol{\beta}^E, \xi) + f(\xi, \eta, \nabla \xi, \nabla \eta) \\ &= W(\boldsymbol{\epsilon}^E, \xi) + f_\xi(\xi) + f_\eta(\eta) + \boldsymbol{\zeta} : \nabla \xi \otimes \nabla \xi + \boldsymbol{\kappa} : \nabla \eta \otimes \nabla \eta. \end{aligned} \tag{3.29}$$

All quantities entering function f are identical to those of Sect. 3.2. The strain energy density is isotropic linear elastic and considers degradation of the shear modulus with cumulative damage ($\xi > 1$):

$$W = \tfrac{1}{2}K(\mathrm{tr}\boldsymbol{\epsilon}^E)^2 + (1 - \xi)^2 \mu \hat{\boldsymbol{\epsilon}}^E : \hat{\boldsymbol{\epsilon}}^E; \qquad \hat{\boldsymbol{\epsilon}}^E = \boldsymbol{\epsilon}^E - \tfrac{1}{3}\mathrm{tr}\boldsymbol{\epsilon}^E \boldsymbol{1}. \tag{3.30}$$

The stress tensor $\boldsymbol{P}$ is symmetric, in lieu of (2.24), and it obeys

$$P^{AB} = \frac{\partial \psi}{\partial \epsilon_{AB}} = \frac{\partial W}{\partial \epsilon^E_{AB}} = K(\epsilon^E)^C_C \delta^{AB} + 2(1 - \xi)^2 \mu (\hat{\epsilon}^E)^{AB}. \tag{3.31}$$

The effective bulk modulus, here taken as constant K, will be permitted to degrade in tension later in Sect. 5. Thermodynamic forces Q_A are computed as follows, instead of (3.19):

$$Q_1 = \frac{1}{l}\frac{\partial \psi}{\partial \xi} = \frac{1}{l}\left[\frac{\partial W}{\partial \xi} + \frac{\partial f_\xi}{\partial \xi} - P^{AB}\frac{\partial \beta^D_{AB}}{\partial \xi}\right], \qquad Q_2 = \frac{1}{l}\frac{\partial \psi}{\partial \eta} = \frac{1}{l}\left[\frac{\partial f_\eta}{\partial \eta} - P^{AB}\frac{\partial \beta^D_{AB}}{\partial \eta}\right]. \tag{3.32}$$

Forces Z^A_B are identical to those of (3.20). The linear momentum balance of (3.23) becomes

$$d_A P^{AB} + P^{AB}(m\xi \partial_A \xi + k\eta \partial_A \eta) = 0. \tag{3.33}$$

Kinetic equations (3.24) are unchanged in form. For the direct energy minimization approach, (3.25) is replaced with

$$\begin{aligned} \min_{\boldsymbol{u}, \boldsymbol{D}} [\Psi(\boldsymbol{u}, \boldsymbol{D})] &= \min_{\boldsymbol{u}, \xi, \eta} \left[\int_{\mathfrak{M}} \psi[\nabla_A u_B(X, t), \xi(X, t), \eta(X, t), \partial_A \xi(X, t), \partial_A \eta(X, t)] \mathrm{d}\Omega\right] \\ &= \min_{\boldsymbol{u}, \xi, \eta} \left[\int_{\mathfrak{M}} \bar{\psi}[\nabla_A u_B(X, t), \xi(X, t), \eta(X, t), \partial_A \xi(X, t), \partial_A \eta(X, t)] \mathrm{d}\Omega_0\right]. \end{aligned} \tag{3.34}$$

The following modified thermodynamic forces (i.e., gradients of energy $\bar{\psi}$) are useful in this context for numerical methods of energy minimization, recalling $\sqrt{G} = \exp[\frac{1}{2}(m\xi^2 + k\eta^2)]$, $D^1 = l\xi$, $D^2 = l\eta$, and $D^3 = 0$:

$$\bar{P}^{AB} = \frac{\partial \bar{\psi}}{\partial \epsilon_{AB}} = P^{AB}\sqrt{G}, \qquad \bar{Q}_A = \frac{\partial \bar{\psi}}{\partial D^A} = Q_A\sqrt{G} + \frac{\bar{\psi}}{2G}\frac{\partial G}{\partial D^A}, \qquad \bar{Z}^A_B = \frac{\partial \bar{\psi}}{\partial(\partial_A D^B)} = Z^A_B\sqrt{G}. \tag{3.35}$$

3.5 Material characteristics

The material of interest in forthcoming applications is boron carbide (B_4C). Material parameters with supporting references or supplementary equation numbers are provided in Table 1. If no reference or equation is listed for a particular row, the reference quoted above it applies.

The particular Cartesian coordinate system introduced in Sect. 3 corresponds to twinning on the $\langle 10\bar{1}0\rangle\{0001\}$ system [6,7,12] and to fracture on basal $\{0001\}$ planes. Amorphous (shear) bands may also form within twinned domains [6,7]. Twinning takes place via coordinated motion of $\langle 10\bar{1}0\rangle$ partial dislocations, with a twinning shear γ_0 estimated as $\frac{2}{3}$a/c [12]. The surface energy resisting twin formation is computed as [66,67]

$$\Gamma = \tau b = \tfrac{1}{3}\tau \mathrm{a}, \tag{3.36}$$

where b is the magnitude of Burgers vector of such partial dislocations and $\tau = 2.9$ GPa is the resolved shear stress needed for twinning [12].

The regularization length l is computed as the cohesive fracture process zone size over which the stress at a (mode II) crack tip degrades [41,48,68]:

$$l = 4\mu\Upsilon/[(1-\nu)\pi\sigma^2], \tag{3.37}$$

where ν is Poisson's ratio and $\sigma \approx \frac{\mu}{2\pi}$ is the theoretical shear strength [14]. The same length is used for regularization of twin and phase boundaries for simplicity, in lieu of other data, and since twinned and amorphous zones are, like the failure process zone, observed to be of widths on the order of nm [1,8].

The pseudo-Finsler metric $\boldsymbol{G}$ measures both densification that accompanies the stress-induced phase transformation from a trigonal crystal to glassy phase [2,4,5,7,9–11,34] as well as dilation associated with fracture or cavitation [7,11]. Weyl transformation factor k is determined from the ratio of mass density of the crystalline phase to that of the glassy phase and use of (3.5) at $\eta = 1$. As in [34], a 4% volume reduction upon structure collapse accompanies total amorphization [2,5,7], dilatation from cavities or fractures is prescribed to precisely offset such densification at $\xi = 1$, leading to the value of $m = -k$ in Table 1. The energy barrier for a quadratic potential is $\hat{A}$ at $\eta = 1$. This value is found from the difference between ground state energy of the most stable B_4C polytype and the energy of segregated elemental phases (boron and amorphous carbon) associated with structure collapse: 0.04 eV [3].

Interpolation function parameters α, β, and χ are chosen such that, consistently with (3.2) and (3.3), initiation of twinning kinematics effectively precedes amorphous densification (i.e., corresponds to a lower value of order parameter η in this case). For example, invoking the values listed in Table 1,

$$\phi_\xi(0.68) = \phi_\eta(0.68) = 0.62, \qquad \phi_0(0.68) = \phi_0(\eta_0) = 0.9, \tag{3.38}$$

noting that the larger the value of ϕ, the more pronounced the contribution from a change in state to deformation in (3.8), (3.9), and (3.10). The final equality in (3.38) is used to establish the value of η_0 in Table 1. From an energetic standpoint, the barrier to twinning transformation is fully overcome at $\eta = \eta_0$ as is clear from (3.16).

The present theory can be used to represent degenerate cases in which one or more inelasticity mechanisms are suppressed by imposing the following conditions:

Table 1 Physical properties and model constants for boron carbide

Property [Units]	Value	Description	Reference
μ [GPa]	193	Shear modulus	[9]
K [GPa]	237	Bulk modulus	
c, a [nm]	1.21, 0.56	Lattice parameters	
Γ [J/m^2]	0.54	Twin boundary surface energy	(3.36)
Υ [J/m^2]	3.27	Fracture surface energy	[69]
l [nm]	0.97	Regularization length	(3.37)
k	-0.0816	Volume reduction (amorphization)	[2,7,34]
m	0.0816	Dilatation (cavitation)	[7]
$\hat{A}$ [GPa]	3.01	Transformation barrier	[3]
γ_0	0.31	Twinning shear	[12]
η_0	0.68	Twinning threshold	(3.38)
α, β, χ	0, 0, 6	Interpolation constants	(3.38)

- Fracture and cavitation suppressed: $\xi(X,t) = 0 \forall X, t$;
- Twinning and amorphization suppressed: $\eta(X,t) = 0 \forall X, t$;
- Amorphization suppressed: $k = 0$, $\hat{A} = 0$;
- Twinning and inelastic shearing (i.e., shear bands) suppressed: $\gamma_0 = 0$, $\Gamma = 0$.

For the final scenario above, it may be realistic to prescribe a gradient coefficient for surface energy of phase boundaries corresponding to the final term in (3.13) in lieu of twin boundary energy, but this is not essential. Finally, kinetic parameters L_ξ and L_η of (3.24) will be discussed later for particular problems.

4 Analysis: simple shear deformation

A fundamental initial boundary value problem is addressed first to demonstrate or validate features of the theory. Specifically, considered here is shearing of a nonlinear elastic slab of boron carbide that may undergo mechanisms of twinning, amorphization, and fracture. Shearing on a basal plane, (0001), in a direction along one of the "a" lattice vectors, $\langle 10\bar{1}0\rangle$, is the intended physical representation. The fully nonlinear version of the theory is used.

4.1 Problem geometry and kinematics

The material manifold is a slab of length L_0 and effectively infinite width and thickness. In three dimensions, $\{\mathfrak{M} : X^1 \in [0, L_0], |X^2| \in \infty, |X^3| \in \infty\}$. Plane strain conditions hold for the X^3-direction. For the spatial configuration, the deformed material manifold is $\{\mathfrak{m} : x^1 \in [0, L], |x^2| \in \infty, |x^3| \in \infty\}$, where L is the deformed length of the domain. In reference and spatial Cartesian coordinates, let $(X^1, X^2, X^3) \to (X, Y, Z)$ and $(x^1, x^2, x^3) \to (x, y, z)$.

Motions, deformations, and state variable gradients defined in Sects. 2 and 3 are computed as follows for simple shear. Let $\varphi = \upsilon + Y$ and γ denote respective motion and strain in the shearing (Y) direction, the latter parallel to twinning direction $\boldsymbol{S}$. Field variables are permitted to vary with X and t, where X is parallel to the basal plane normal vector $\boldsymbol{M}$. The out-of-plane coordinate is Z. Then

$$x = X, \quad y = \varphi(X,Y,t) = Y + \upsilon(X,t), \quad z = Z; \qquad \xi = \xi(X,t), \quad \eta = \eta(X,t); \tag{4.1}$$

$$\begin{aligned} \boldsymbol{F}(X,t) &= \begin{bmatrix} \partial x(X)/\partial X & \partial x(X)/\partial Y & \partial x(X)/\partial Z \\ \partial \varphi(X,Y,t)/\partial X & \partial \varphi(X,Y,t)/\partial Y & \partial \varphi(X,Y,t)/\partial Z \\ \partial z(Z)/\partial X & \partial z(Z)/\partial Y & \partial z(Z)/\partial Z \end{bmatrix} \\ &= \begin{bmatrix} 1 & 0 & 0 \\ \partial \upsilon(X,t)/\partial X & 1 & 0 \\ 0 & 0 & 1 \end{bmatrix} = \begin{bmatrix} 1 & 0 & 0 \\ \gamma(X,t) & 1 & 0 \\ 0 & 0 & 1 \end{bmatrix}; \end{aligned} \tag{4.2}$$

$$J = \det \boldsymbol{F} = F_1^1 F_2^2 F_3^3 = F_X^x F_Y^y F_Z^z = 1. \tag{4.3}$$

The total shear strain is $\gamma(X,t)$, and volume is conserved. The first of (4.1) suggests $L = L_0$.

Now the multiplicative kinematic description of Sect. 3.1 is specialized to the case of simple shear that is of focus in Sects. 4.2 and 4.3. The total deformation gradient is the product

$$\begin{aligned} \boldsymbol{F}(X,t) &= \begin{bmatrix} 1 & 0 & 0 \\ \gamma(X,t) & 1 & 0 \\ 0 & 0 & 1 \end{bmatrix} = \boldsymbol{F}^E(X,t)\boldsymbol{F}^D[D(X,t)] \\ &= \begin{bmatrix} (F^E)_X^x(X,t) & 0 & 0 \\ (F^E)_X^y(X,t) & (F^E)_Y^y(X,t) & 0 \\ 0 & 0 & (F^E)_Z^z(X,t) \end{bmatrix} \begin{bmatrix} F^\xi(X,t)\bar{F}^\eta(X,t) & 0 & 0 \\ 0 & F^\xi(X,t) & 0 \\ 0 & 0 & F^\xi(X,t) \end{bmatrix} \begin{bmatrix} 1 & 0 & 0 \\ \gamma^D(X,t) & 1 & 0 \\ 0 & 0 & 1 \end{bmatrix}. \end{aligned} \tag{4.4}$$

Inelastic deformations in the present coordinate system are represented by the scalar components

$$F^\xi(\xi) = 1 + x_\xi \phi_\xi(\xi), \qquad \bar{F}^\eta(\eta) = 1 + x_\eta \phi_\eta(\eta), \qquad \gamma^D(\eta) = \gamma_0 \phi_0(\eta). \tag{4.5}$$

The inelastic volume change is found from (3.12). The elastic volume ratio J^E and the elastic shear strain γ^E are then, from (4.2)–(4.5),

$$J^E(\xi,\eta) = [1 + x_\xi \phi_\xi(\xi)]^{-3}[1 + x_\eta \phi_\eta(\eta)]^{-1}, \qquad \gamma^E(\eta, X, t) = \gamma(X,t) - \gamma^D(\eta). \tag{4.6}$$

Gradients of state variable components (i.e., order parameter gradients) are simply noted as

$$\xi'(X,t) = \partial \xi(X,t)/\partial X, \qquad \eta'(X,t) = \partial \eta(X,t)/\partial X. \tag{4.7}$$

4.2 Governing transient equations

For the present loading protocol, the energy density of (3.13) becomes

$$\psi(\gamma,\xi,\eta,\xi',\eta') = W[\boldsymbol{C}^E(\gamma^E,\xi,\eta),\xi] + f_\xi(\xi) + f_\eta(\eta) + \Upsilon l(\xi')^2 + \tfrac{3}{4}\Gamma l(\eta')^2. \tag{4.8}$$

The stress tensor $[P_{aA}]$ of (3.18) in matrix form is

$$\begin{aligned}\boldsymbol{P} = {}& \mu(1-\xi)^2(J^E)^{2/3}\frac{1}{(F^\xi\bar{F}^\eta)^2}\begin{bmatrix}1 & -\gamma^D & 0\\ \gamma^E & 1-\gamma^E\gamma^D & 0\\ 0 & 0 & (\bar{F}^\eta)^2\end{bmatrix}\\ & -\mu(1-\xi)^2(1+\tfrac{2}{3}\ln J^E)\begin{bmatrix}1 & -\gamma & 0\\ 0 & 1 & 0\\ 0 & 0 & 1\end{bmatrix} + K\ln J^E\begin{bmatrix}1 & -\gamma & 0\\ 0 & 1 & 0\\ 0 & 0 & 1\end{bmatrix}.\end{aligned} \tag{4.9}$$

Forces Q_A in (3.19) are computed in a straightforward manner but are too lengthy to list conveniently in explicit form. Forces in (3.20) simply reduce to

$$Z_1^1 = 2\Upsilon\xi', \qquad Z_2^1 = \tfrac{3}{2}\Gamma\eta'. \tag{4.10}$$

The balance of linear momentum for stresses in (3.23) reduces to two equations, with fields depending on (X,t):

$$d_1P_{11} + P_{11}(m\xi\xi' + k\eta\eta') = 0, \qquad d_1P_{21} + P_{21}(m\xi\xi' + k\eta\eta') = 0. \tag{4.11}$$

The first kinetic equation in (3.24) reduces to

$$\dot{\xi} = -(\mathsf{L}_\xi l^2/\Upsilon)\left[Q_1 - 2\Upsilon\xi'' - 2\Upsilon\xi'(m\xi\xi' + k\eta\eta') + 2m\xi\psi/l\right]. \tag{4.12}$$

Coherent structural transformations such as twinning or phase changes are assumed here to occur much faster than damage evolution, similar to what is observed in dynamic atomic simulations [7]. It would be mathematically possible to introduce kinetic equations for the former, but this approach is not pursued here in order to limit the number of possible solutions to a number feasible for detailed analysis. Thus, energy minimization is invoked to obtain the solution field $\eta(X,t)$ via (3.25), which reduces here to

$$\min_{\boldsymbol{x},\boldsymbol{D}}[\Psi(\boldsymbol{\varphi},\boldsymbol{D})] \to \min_{\eta(X,t)\in[0,1]}\left[\int_{\mathfrak{M}}\bar{\psi}[\gamma(X,t),\xi(X,t),\eta(X,t),\xi'(X,t),\eta'(X,t)]\mathrm{d}\Omega_0\right]. \tag{4.13}$$

Particular solutions depend on initial and boundary conditions as will be discussed in what follows next.

4.3 Solutions: homogeneous case

Sought first are solutions for which internal state variable fields are spatially homogeneous, often denoted by an H subscript:

$$\xi(X,t) = \xi_H(t), \qquad \eta(X,t) = \eta_H(t). \tag{4.14}$$

Initial and boundary conditions on order parameters are

$$\xi(X,0)=\xi_H(0)=0, \quad \eta(X,0)=\eta_H(0)=0; \qquad \xi(0,t)=\xi(L_0,t)=\xi_H(t), \quad \eta(0,t)=\eta(L_0,t)=\eta_H(t). \tag{4.15}$$

Values of ξ_H and η_H that vary with time t will be obtained explicitly as an outcome of the forthcoming solution procedure. Initial and boundary conditions on shear displacement $\upsilon(X,t)$ are

$$\upsilon(X,0) = 0; \qquad \upsilon(0,t) = 0, \quad \upsilon(L_0,t) = \upsilon_L(t) = \dot{\gamma}tL_0. \tag{4.16}$$

The applied shear strain rate is written as the constant $\dot{\gamma}$. Since $\xi' = \eta' = 0$ in (4.7), linear momentum balances (4.11) yield

$$d_1P_{11} = 0 \Rightarrow P_{11}(t) = \text{constant}, \qquad d_1P_{21} = 0 \Rightarrow P_{21}(t) = P(t) = \text{constant}, \tag{4.17}$$

where $P(t)$ is used to denote the homogeneous shear stress at time t. Since order parameters, i.e., $\boldsymbol{D}$, are constant at time t, $\boldsymbol{F}^D(t) = \text{constant}$, $\boldsymbol{F}^E(t) = \text{constant}$, the energy density ψ and all other stress components are also constants at t, and the imposed shear strain is homogeneous over the domain:

$$\gamma(X,t) \to \gamma(t) = \dot{\gamma} t. \tag{4.18}$$

The reference pressure, positive in compression, is defined as

$$p(t) = -\tfrac{1}{3}[P_{11}(t) + P_{22}(t) + P_{33}(t)]. \tag{4.19}$$

The kinetic equation for fracture or cavitation in (4.12) reduces to

$$\dot{\xi}(t) = -(\mathsf{L}_\xi l^2/\Upsilon)\,[Q_1(t) + 2m\xi(t)\psi(t)/l] = -10^r\,(\dot{\gamma} l^2/\Upsilon)\,[Q_1(t) + 2m\xi(t)\psi(t)/l]\,, \tag{4.20}$$

where r is a dimensionless variable controlling the rate of damage evolution (kinetic rate) relative to the applied strain rate. In later calculations, the discrete values $r = 0, 1, 2, 3, 4$ are considered parametrically since known experimental or atomic simulation data do not provide specific values. At each time increment, the value of $\eta(t)$ is obtained by solving the minimization problem in (4.13) which now reduces to

$$\min_{\eta(t)\in[0,1]}\left[\int_0^{L_0} \bar{\psi}[\gamma(t),\xi(t),\eta(t)]\mathrm{d}X\right] \to \min_{\eta(t)\in[0,1]}\left[\psi[\gamma(t),\xi(t),\eta(t)]\sqrt{G[\xi(t),\eta(t)]}\right]. \tag{4.21}$$

In practice, kinetic equation (4.20) is numerically evaluated by explicit integration. At each time increment, stress components are computed from (4.9), driving forces are computed from (3.19), and energy density is computed from (4.8) with $\eta' = \xi' = 0$ for the present homogeneous field solutions. Simultaneously, the order parameter $\eta(t)$ is found by searching the domain $\eta \in [0, 1]$ for that value which minimizes the free energy density $\bar{\psi} = \psi\sqrt{G}$ as in (4.13). The values of $\xi(t)$ and $\eta(t)$ obtained in this staggered matter can be interpreted as time-dependent boundary conditions in (4.14).

Results for the case with all inelastic mechanisms enabled—twinning, phase changes, and fracture—are shown in Fig. 1. Recall that this situation corresponds physically to shear deformation of a boron carbide single crystal along $(0001)\langle 10\bar{1}0\rangle$. In all subfigures, results are depicted versus applied shear γ. As shown in Fig. 1a, the order parameter associated with twinning and amorphization, η, acquires a positive (nonzero) value at a relatively low applied strain of $\gamma \approx 0.01$, then increases rapidly to $\eta = 0.8$ with increasing γ, attaining $\eta = 0.7$ at $\gamma \approx 0.31 \approx \gamma_0$, where γ_0 is the eigenstrain from twinning shear in Table 1. Evolution of η at larger applied strain $\gamma \gtrsim 0.36$ depends on the of choice of damage kinetic parameter r in this case. For $r \leq 2$, i.e., slow damage growth, η attains a maximum value of unity at large applied shear, whereas for $r \geq 3$, this order parameter attains maxima not exceeding $\eta \approx 0.9$. The order parameter associated with fracture, ξ, is reported in Fig. 1b. Fracture (measured by increasing ξ) occurs more rapidly with increasing r but does not commence until $\eta \geq 0.7$, i.e., upon $\approx 90\%$ saturation of shear accommodation from twinning. Shear stress P normalized by the shear modulus is shown in Fig. 1c. Results labeled "elastic" correspond to the nonlinear elastic solution with $\eta = \xi = 0$, i.e., $P = \mu\gamma$. Shear stress is relaxed by twinning in each case for $\gamma \leq \gamma_0$ and further reduced by damage ($\xi > 0$) at larger γ. The larger the value of r, the greater the relaxation due to fracture, as manifested by a drop in tangent shear modulus $\mu(1-\xi)^2$. Twinning initiates at $P/\mu \approx 0.01$ or a resolved shear stress of about 1.7 GPa, which is reasonably close to the value of $\tau = 2.9$ GPa reported in experiments [12] but an order of magnitude smaller than the values on the order of $\mu/10$ reported from atomic simulations [6,7]. Pressure p of (4.19) is shown in Fig. 1d. For small $\gamma \lesssim \gamma_0$, pressure p is increasingly negative (tensile) as amorphization takes place, since inelastic densification from this phase change is offset by elastic tensile deformation to maintain a state of simple shear with $J = 1$ in (4.3). Subsequently, the tensile pressure is reduced in magnitude with increasing γ, noting that cavitation represented by $\xi > 0$ leads to dilatation that offsets densification from amorphization and relaxes the otherwise tensile elastic volume change. This sequence of mechanisms—twinning, amorphization, and cavitation—and corresponding pressure evolution is similar, qualitatively, to mechanisms observed in atomic simulations [6,7]. Energy density ψ normalized by the shear modulus is shown in Fig. 1e. Trends are similar to those reported for shear stress P in Fig. 1c. The energy of the perfectly elastic case, $\psi = \frac{1}{2}\mu\gamma^2$, equals or exceeds that for all of the other solutions, meaning that the other solutions are energetically stable over the elastic one which also satisfies the governing equations of static equilibrium.

Hypothetical problems wherein one or more inelastic deformation mechanisms are suppressed are now addressed. First consider the case in which amorphization is prohibited but twinning and fracture are enabled.

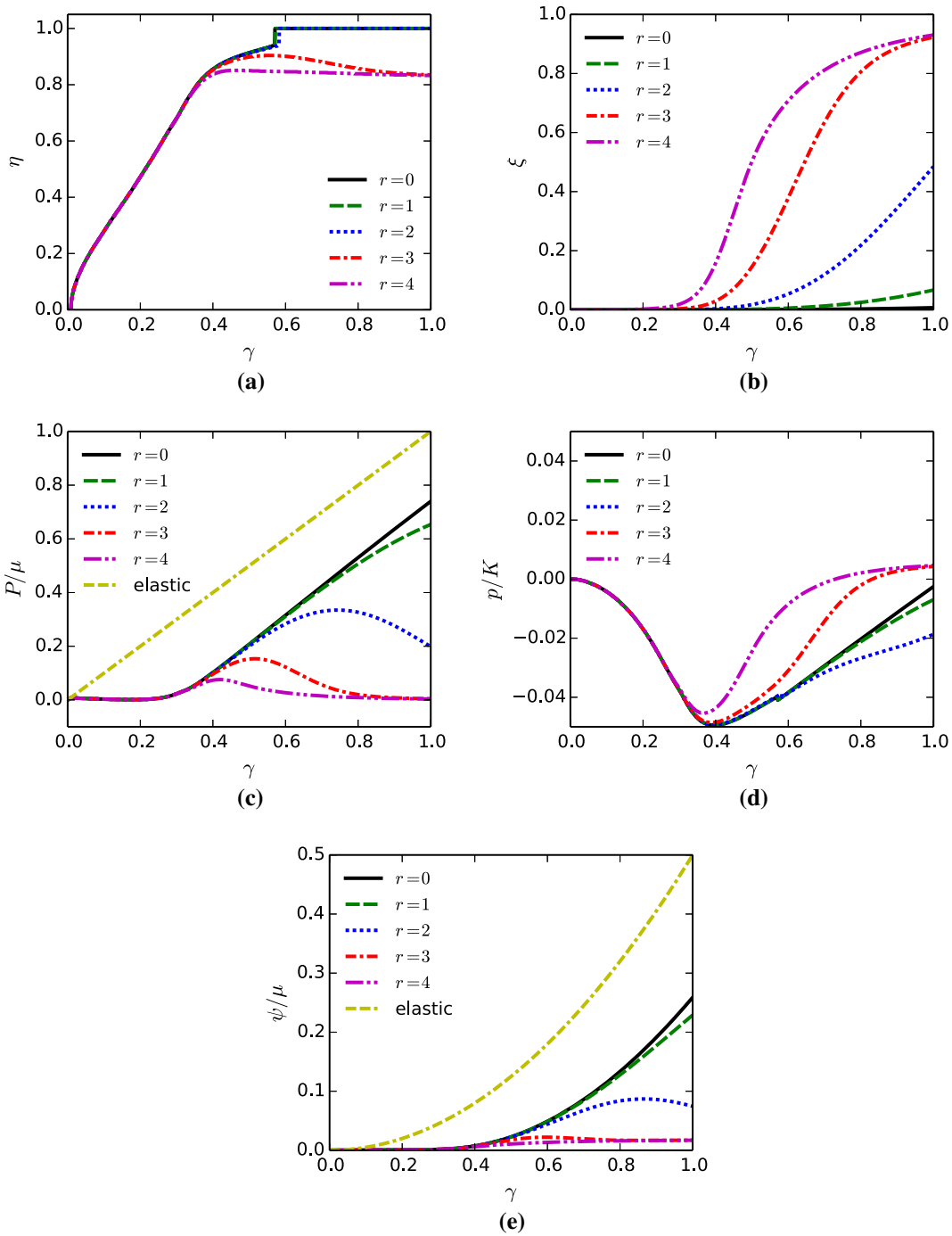

Fig. 1 Homogeneous simple shear, all inelasticity mechanisms active **a** twinning-amorphization parameter **b** fracture parameter **c** shear stress **d** nominal pressure **e** total energy density

This corresponds to setting $A = 0$ and $k = 0$ in the theory of Sect. 3, disabling the quadratic potential associated with solid–solid phase change and the contribution to volumetric deformation and the material metric from densification accompanying this change. Results are given in Fig. 2, with content in each subfigure analogous to those in Fig. 1. Except for evolution of η and p, differences in results with amorphization suppressed are not highly discernible compared to those in Fig. 1 in which all inelastic mechanisms are permissible. Regarding η, as shown in Fig. 2a, the order parameter associated with twinning acquires a positive (nonzero) value at a relatively low applied strain of $\gamma \approx 0.02$, then increases rapidly to $\eta = 1$ with increasing γ, attaining $\eta = 1$ at

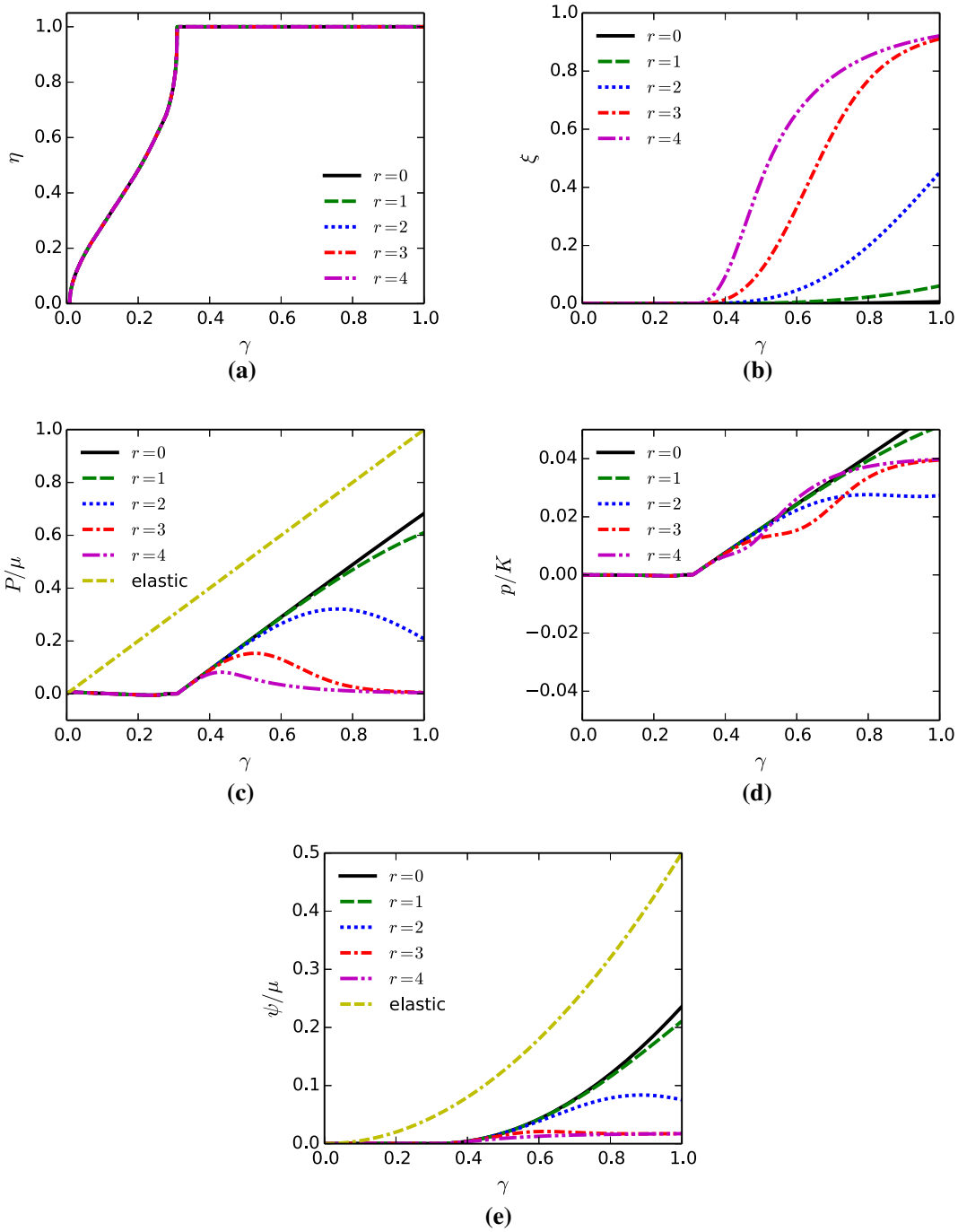

Fig. 2 Homogeneous simple shear, amorphization suppressed **a** twinning parameter **b** fracture parameter **c** shear stress **d** nominal pressure **e** total energy density

$\gamma \approx 0.3 \approx \gamma_0$. Twinning in the absence of phase change initiates at $P/\mu \approx 0.02$ or a resolved shear stress of about 3.3 GPa, very close to the value of $\tau = 2.9$ GPa reported in [12]. A notable exception/difference is the reference pressure in Fig. 2d, which does not demonstrate a tensile (negative) portion prior to attainment of $\gamma \approx \gamma_0 \approx 0.3$, in contrast to p in Fig. 1d. The difference is due to the omission of densification in the former (Fig. 2d): nearly all deformation is accommodated by twinning at low applied shear strain, which is isochoric, resulting in null pressure change. The onset of damage reflected by $\xi > 0$ is delayed slightly in the present case in Fig. 2b with amorphization suppressed relative to results in Fig. 1b.

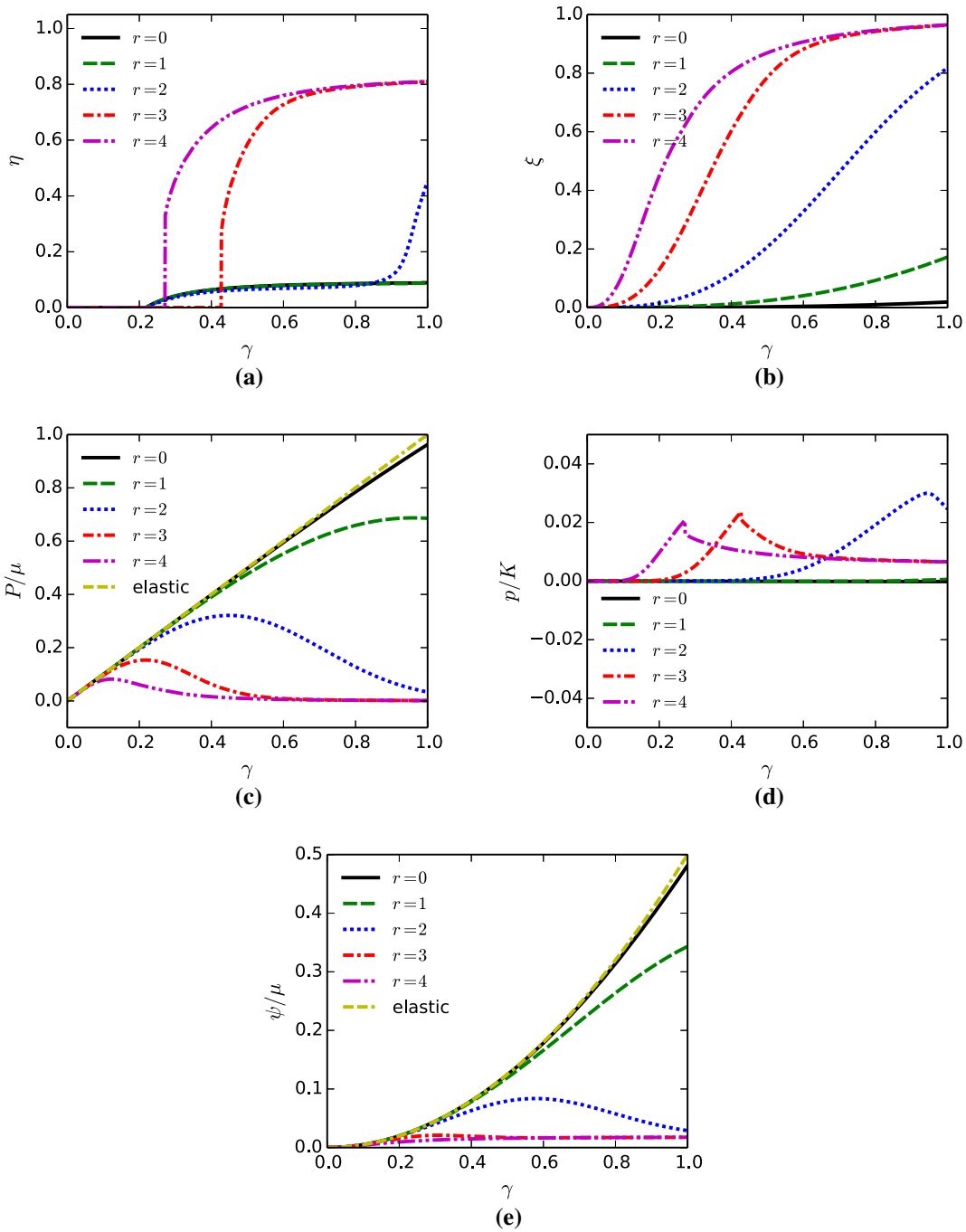

Fig. 3 Homogeneous simple shear, twinning suppressed **a** amorphization parameter **b** fracture parameter **c** shear stress **d** nominal pressure **e** total energy density

Presented in Fig. 3 are results corresponding to omission of deformation twinning but allowing for amorphization and fracture/cavitation. In boron carbide, such results would pertain to a deformation system such as $\langle \bar{1}101\rangle(01\bar{1}\bar{1})$ wherein atomic simulations predict the same physical mechanisms [6,7]. In the theory of Sect. 3, twinning is disabled by setting $\gamma_0 = 0$ in the kinematics and $\Gamma = 0$ in energy contribution f_0. In this case, η solely depicts transformation from crystal to glass, with predicted evolution given in Fig. 3a. Transformation behavior is strongly coupled to fracture kinetics: the choice of r affects how readily fracture with $\xi > 0$ occurs in Fig. 3b, and thus the value of γ at which an abrupt transformation from crystal to glass ($\eta > 0$) takes place.

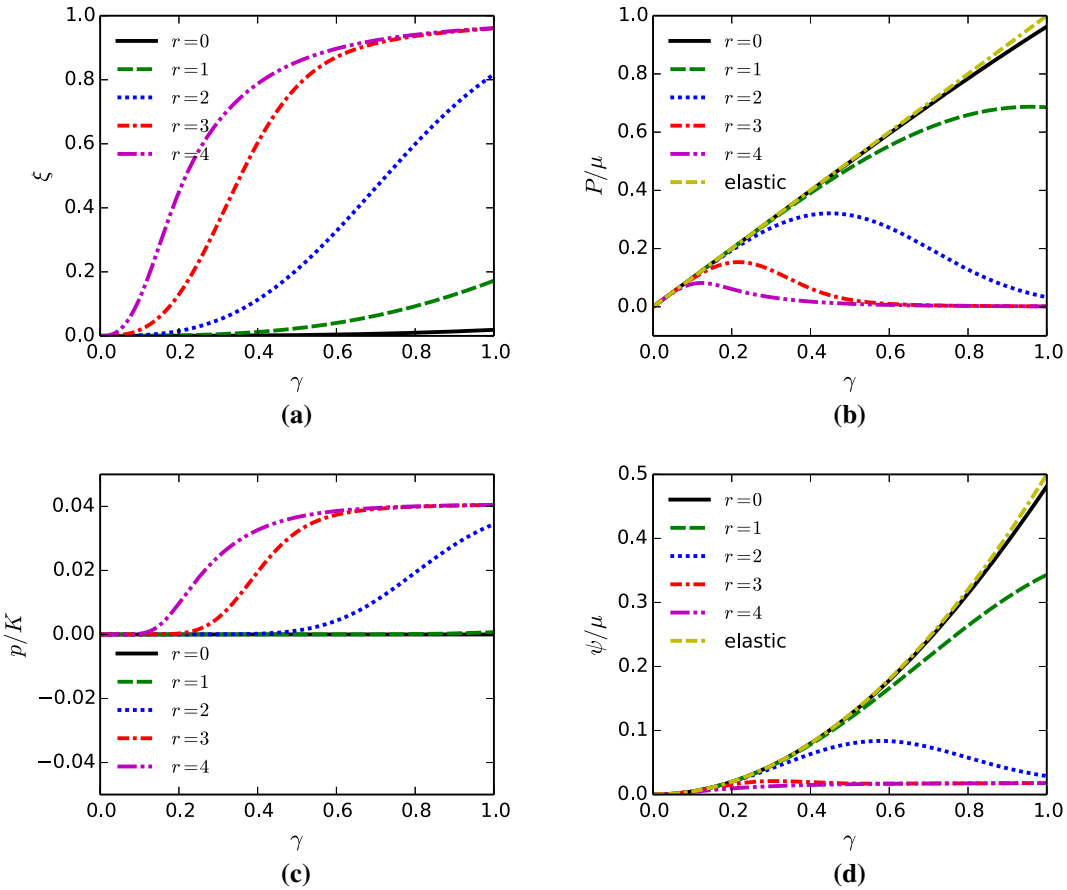

Fig. 4 Homogeneous simple shear, twinning and amorphization suppressed **a** fracture parameter **b** shear stress **c** nominal pressure **d** total energy density

Interestingly, the tendency for the onset of earlier amorphization does not always increase with increasing r. Comparing Fig. 3b with Fig. 1b, fracture usually takes place at a much lower applied strain γ when twinning is suppressed, since inelastic shear accommodation does not occur. Curves for shear stress in Fig. 3c and energy density in Fig. 3e are offset leftwards relative to their counterparts in Fig. 1c, e for this reason, i.e., since the rather flat parts of each curve in Fig. 1 are missing in Fig. 3 when twinning does not take place. Pressure in Fig. 3d follows rather complex behavior due to the simultaneous competing volume changes induced by phase change (densification) and cavitation (expansion), but tensile (negative) pressures are never attained since cavitation alleviates any tensile stress. For the case $r = 0$, energy density in Fig. 3e is very close to that for the elastic solution, while for $r > 0$, ψ is increasingly exceeded by that of the elastic solution with increasing γ. Comparing Fig. 3a with Fig. 2a, η begins rapidly increasing at a much lower applied strain γ for the latter case where η represents isolated twinning versus the former case where η represents isolated amorphization. In other words, the model realistically [7] predicts that twinning should precede amorphization under simple shear loading for boron carbide when either mechanism is permissible to occur independently of the other.

Finally, results in Fig. 4 demonstrate model capabilities when both twinning and phase changes are suppressed. Physically, this would represent deformation on a plane and in a direction different than those reported in experiments [1] and atomic simulations [6,7] that do exhibit such coherent structural changes. One such plane and set of directions is $\langle 1\bar{1}00\rangle(1100)$ [6]. In the theory of Sect. 3, suppression of twinning and amorphization is effected by setting $\eta(t) = 0 \forall t$. Thus, Fig. 4 contains only four parts, as opposed to Figs. 1, 2, and 3, since there is no need to present evolution of η here. Similar to results in Fig. 3b, evolution of ξ in Fig. 4a depends strongly on the choice of kinetic parameter r, with larger r speeding the increase in damage accumulation. Shear stress in Fig. 4b reaches a lower maximum and then decreases more rapidly the larger the value of r as expected, recalling that the effective shear modulus of the theory is $\mu(1-\xi)^2$. Pressure in Fig. 4c is negligible for cases with small r (i.e., $r \leq 1$), but increases with increasing ξ for the other cases since

cavitation is offset by elastic compression to maintain a state of simple shear with total volume ratio $J = 1$. Energy density in Fig. 4d follows similar trends as the shear stress reported in Fig. 4b.

4.4 Solutions: stress-free case

The same domain considered in Sect. 4.1 is addressed here, but solutions now require vanishing stress components, i.e., $P_a^A = 0 \forall X \in [0, L_0]$. The strain energy density W vanishes correspondingly. Restriction to the static case is also invoked, meaning time is held fixed and is thus effectively omitted from the governing equations.

For the internal state or order parameter ξ, complete shear failure of the slab is assigned at $X = 0$, with the opposite end at $X = L_0$ undamaged. Boundary conditions on the order parameter $\xi(X)$ are thus

$$\xi(0) = 1, \qquad \xi(L_0) = 0. \tag{4.22}$$

For the order parameter η, two conditions are considered that both result in null contributions to energy potentials f_η and ψ. The first sets $\eta(X) = 0 \forall X$, while the second sets $\eta(X) = 1 \forall X$. The slab of material is assigned shear deformation boundary conditions $\upsilon(0) = 0$ and $\upsilon(L_0) = \upsilon_L = \gamma L_0$, with $\gamma =$ constant the imposed shear displacement. Within the domain $X \in (0, L_0)$, arbitrary deformation is permitted to maintain a stress-free state, as implied but not explicitly stated in some similar prior work [46]. Complete separation of the slab at $X = 0$ may occur where $\xi = 1$ such that rigid body motion enables satisfaction of the displacement boundary condition at $X = L_0$. Solutions with vanishing stress automatically satisfy the macroscopic linear momentum balance.

For the static case, $\dot{\xi}/\mathsf{L}_\xi \to 0$ in (4.12), such that the terms in square brackets vanish identically at equilibrium, which would correspond to rate parameter $r \to \infty$. Noting again that $W = 0$ for the stress-free problem, the resulting governing equation is

$$\xi'' - \xi/l^2 + m\xi[(\xi')^2 - f/(\Upsilon l)] = 0 \Rightarrow \xi'' = (\xi/l^2)(1 + m\xi^2). \tag{4.23}$$

A transformation of variables $\zeta = \xi'$ is now used to restate the above second-order ordinary differential equation. Then $\xi'' = \zeta \cdot \mathrm{d}\zeta/\mathrm{d}\xi$, and (4.23) becomes a non-homogeneous first-order differential equation and general solution

$$\zeta \mathrm{d}\zeta = (\xi/l^2)(1 + m\xi^2)\mathrm{d}\xi \Rightarrow \zeta = \pm(\xi/l)\sqrt{1 + m\xi^2/2 + c_1/\xi^2}. \tag{4.24}$$

Here integration constant $c_1 = 0$, and only the negative root is appropriate. The rightmost expression in (4.24) is integrated for an implicit solution of $\xi(X)$, evaluated numerically:

$$\mathrm{d}\xi = -(\xi/l)\sqrt{1 + m\xi^2/2}\,\mathrm{d}X \Rightarrow X(\xi) = \int_1^\xi \frac{-l\mathrm{d}\beta}{\beta\sqrt{1 + m\beta^2/2}}. \tag{4.25}$$

The total free energy per unit cross-sectional area of the original slab is defined as the line integral

$$\Psi_F = \int_0^{L_0} \psi \mathrm{d}X = \int_0^{L_0} \Upsilon[(\xi')^2 l + \xi^2/l]\mathrm{d}X. \tag{4.26}$$

Profiles of the damage state variable for a domain size of $L_0 = 10l$ are shown in Fig. 5a, b, with the latter focused on that portion of the domain close to the fully failed end at $X = 0$. Weyl scaling parameter m is varied over a suitable range $m \in [2\ln 0.96, -2\ln 0.96]$. The particular value of $m = +0.0816$ is physically realistic for cavitation as used in Sect. 4.3, while $m = -0.0816$ would correspond to $m \to k$ of Table 1 and a density increases with amorphization. When $m = 0$, the metric no longer depends on internal state, and the theory becomes similar to a phase field representation [64]. The magnitude of ξ decreases rapidly from $\xi = 1$ at $X = 0$ with increasing X, and this trend is independent of m. Effects of m on the ξ field thus appear almost negligible. The total energy per unit cross-sectional area of the slab in the YZ-plane from (4.26) is listed for two different values of l/L_0 in columns 2 and 3 of Table 2, normalized by failure surface energy Υ. Total energy Ψ_F increases very slightly with increasing magnitude $|m|$ in each column, with the minimum value corresponding to $m = 0$. A result of $\Psi_F = \Upsilon$ would be equivalent to a Griffith-type theory of perfectly brittle mode II fracture. As l/L_0 decreases, convergence of Ψ_F toward the this value is evident, irrespective

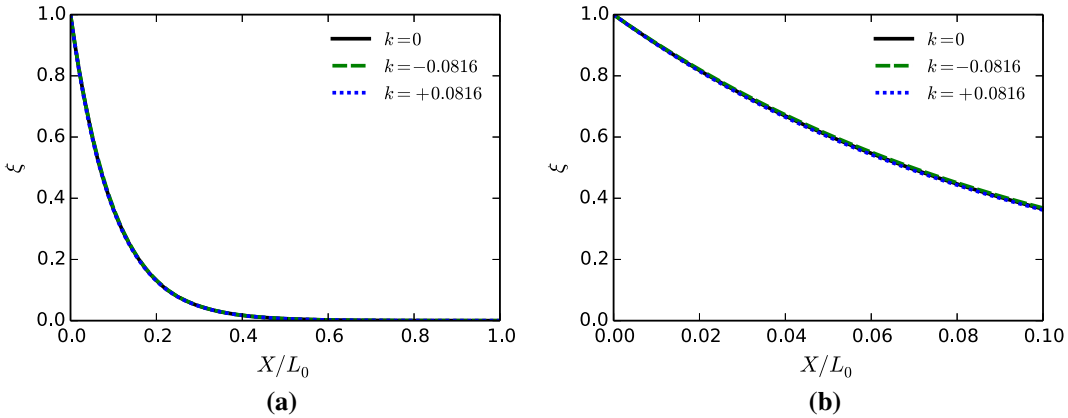

Fig. 5 Shear fracture, stress-free solutions, $l/L_0 = 0.1$ **a** ξ: $0 \le X \le L_0$ **b** ξ: $0 \le X \le 0.1L_0$

Table 2 Boron carbide, stress-free solutions for $l/L_0 = 0.1$ and $l/L_0 = 10^{-3}$: energy Ψ_F, shear displacement υ_C, and shear stress P_C for favorable transition from homogeneous to localized solutions

Weyl scaling factor	Ψ_F/Υ $l = 0.1L_0$	Ψ_F/Υ $l = 10^{-3}L_0$	υ_C/L_0 $l = 0.1L_0$	P_C/μ $l = 0.1L_0$
$m = -0.0816$	1.009183	1.000064	0.486	0.193
$m = 0$	1.009109	0.999992	0.485	0.191
$m = +0.0816$	1.009178	1.000060	0.486	0.193

of the value of $m \in [-0.0816, +0.0816]$. This trend agrees with results in prior works that consider a slightly different form of Weyl scaling of the material metric.[1]

Relative stability of homogeneous solutions of Sect. 4.3, with all inelasticity mechanisms enabled and $r \le 3$, versus localized stress-free solutions of the present section is characterized by the rightmost two columns of Table 2. Transition from a homogeneous state to a stress free, fully fractured state is energetically favorable at an applied deformation $\upsilon_L \ge \upsilon_C$. The value of υ_C is attained when the homogeneous total energy $\Psi_H = \psi L_0$ obtained from the analysis of Sect. 4.2 equals or exceeds Ψ_F of (4.26). At such a transition point the homogeneous solution becomes relatively unstable. Shear stress at the onset of instability is denoted by P_C. From Table 2, shear strain υ_C/L_0 is on the order of 0.5 and stress $P_C \approx 37$ GPa is on the order of 20% of the initial shear modulus μ, irrespective of m.

4.5 Summary of results for simple shear deformation

Essential findings of the semi-analytical results for B_4C are summarized in the points below:

- The model predicts the energetically preferred sequence of inelastic mechanisms of twinning followed by amorphization followed by fracture, in agreement with atomic simulation [6] of shearing on $\langle 10\bar{1}0\rangle(0001)$;
- The model predicts a shear stress of 3.3 GPa needed to initiate deformation twinning in the absence of phase changes, in fair agreement with the experimental estimate of 2.9 GPa [12];
- The model predicts tensile pressure commensurate with amorphization that is later relieved by dilatation from cavitation, in agreement with atomic simulations [6];
- The model demonstrates convergence to the correct mode II failure energy with decreasing regularization length l for a physically realistic range of Weyl scaling parameter m;
- The model's predictions for homogeneous deformation with inelastic mechanism(s) enabled are all energetically stable with respect to homogeneous fully elastic deformation, and a transition from homogeneous deformation to localized shear fracture becomes energetically favorable at an applied shear strain of

[1] In [41,44–46], a metric with determinant of the form $G(\xi) = \exp(2m\xi)$ was considered, leading to solutions of the here-corrected form $X(\xi) = \int_1^\xi (-l\,\mathrm{d}\beta)/(\beta\sqrt{1+2m\beta/3})$. Trends in results reported in those references are unchanged and agree with those corresponding to the current analysis of Sect. 4.4.

$\gamma \approx 0.49$ and stress of $P \approx 37$ GPa. These values of shear strain and failure stress are similar to theoretical maximums observed in atomic simulations [6,7].

Importantly, results presented in Sect. 4 are obtained without any fitting/calibration of parameters to explicitly match data from any external sources: all parameters in Sect. 3.5 are specified a priori, noting that the relative rate of damage kinetics is varied parametrically.

5 Numerical simulations

Analytical or semi-analytical solutions are generally unavailable for general three-dimensional boundary value problems due to the complexity of the constitutive model. Advanced numerical methods of solution are implemented here via the finite element (FE) method.

5.1 Finite element method

In this work, FE solutions are limited to those of quasi-statics, whereby boundary conditions are updated incrementally as the analysis proceeds. The geometrically linear theory is used for computational efficiency, with global energy minimization applied toward solution of the discretized problem. More specifically, the static equilibrium equations are those of Sect. 3.4, (3.34) and (3.35). The algorithms invoked herein are similar to those implemented in [50]. A notable difference is the presence of the scaling factor $\sqrt{G}$ in the energy functional of (3.34) and conjugate forces in (3.35) that is absent in the phase field models implemented previously [31,36,50].

Recall from prior discussion in Sect. 3.1 that components of the internal state vector $\boldsymbol{D}$, when normalized by the regularization length l, are identified with two order parameters $\xi(X)$ and $\eta(X)$, where dependence on all three Cartesian coordinates is implicit in the notation, e.g., $\eta(X)$ is shorthand for $\eta(X, Y, Z)$ in the present context. In the FE implementation, each node supports five degrees-of-freedom: three components of displacement $\boldsymbol{u}$ and the aforementioned two order parameters. Boundary conditions for displacement $\boldsymbol{u}$ and order parameters (or their conjugate forces) are updated during each load increment. Candidate solutions, i.e., fields $\boldsymbol{u}(X)$, $\xi(X)$, and $\eta(X)$, are obtained that minimize total system energy Ψ subjected to boundary constraints. Because Ψ is generally non-convex, multiple (local) minima may exist, and solutions may be non-unique. For cases when Ψ of such a local minima exceeds the global minimum energy, then such a solution is said to be "metastable". First and second derivatives of energy density with respect to displacements, order parameters, and their gradients are used in the algorithms implemented for conjugate gradient energy minimization, similarly to those in [50]. The preconditioned conjugate gradient method for nonlinear equations is invoked, specifically the Polak–Ribiere variant of the conjugate gradient technique with the secant method for line searching. Because all degrees-of-freedom are sought or solved for simultaneously, Jacobi preconditioning provides accelerated convergence.

As in prior work [31,50], to ensure irreversibility of crack extension, constraints $\delta\xi(X) \geq 0$ for $\xi(X)$ exceeding a threshold value are imposed. Similarly, to make twinning and phase changes irreversible, $\delta\eta(X) \geq 0$ for $\eta(X)$ exceeding a threshold are imposed. Otherwise, these deformation mechanisms would become thermodynamically reversible and highly damaged or transformed zones in the material could unrealistically disappear on unloading. (However, in some cases reversible twinning or phase changes may not be unrealistic depending on the material and loading, as will be discussed later in the context of numerical results.) Threshold values are taken as 0.9 in subsequent simulations, as in [50]. With such constraint(s) active, the incremental energy minimization problem can be viewed as minimization of energy of an alternative system with time-dependent boundary conditions associated with introduction of new free surfaces along which $\xi \geq 0.9$ is prescribed, with analogous interpretation and conditions for irreversible phase changes. The local equilibrium equations remain satisfied in solutions obtained for this alternative system.

As shown in Fig. 6, a synthetic microstructure of a polycrystal with equi-axed grains is considered, similar to those in prior work [49]. Volume meshes are created from stereolithographic (STL) files of surface representations of grains comprising the microstructure. A three-dimensional volume mesh of hexahedral continuum finite elements is then created within the surface mesh of every crystal in the aggregate. The polycrystal in Fig. 6 consists of 50 grains. The body is a cube of dimensions $L \times L \times L$. In a global Cartesian system, one corner is fixed at $(X, Y, Z) = (0, 0, 0)$, and the opposite corner is initially located at $(X, Y, Z) = (L, L, L)$. Average grain sizes are estimated as $L/4$. In the present application, $L = 100$ nm, so average grains are sized

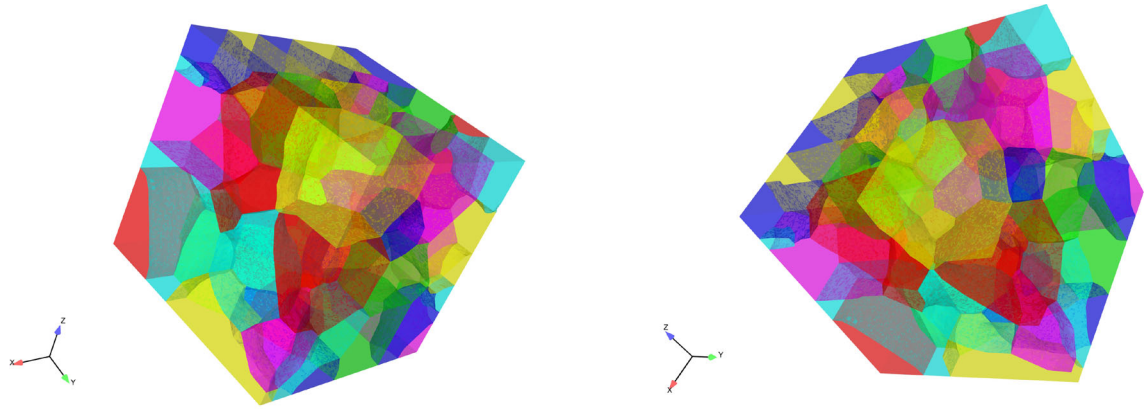

Fig. 6 Polycrystalline microstructure, two views **a**, **b** referred to a global (X, Y, Z) coordinate frame

on the order of 25 nm, which is about two orders of magnitude smaller than the average grain size of boron carbide polycrystals obtained from conventional processing [70]. Presently, computing restrictions render consideration of a polycrystal with grains of micron-scale dimensions impossible if a realistic regularization length on the order of $l \approx 1$ nm is used (Table 1) since the element size cannot reasonably exceed the regularization length.

The FE mesh contains $\approx$ 3.5M elements, and it is sufficiently refined to resolve grain boundary surface morphology, the regularization length, and gradients of field variables when $2 \times 2 \times 2$ integration (8 Gauss points per element) is invoked. Reduced integration was found inadequate, on the other hand, for the present set of model parameters. In the present simulations, perfectly bonded grains are considered, restricting fractures to transgranular or cleavage type, though stress concentrations from cleavage plane orientation mismatch at grain boundaries may affect failure.

The constitutive model of Sect. 3 is invoked, noting that preferred planes and directions correspond to orientations of a local Cartesian coordinate frame assigned to each crystal in the aggregate. Each crystal is assigned a single plane $\boldsymbol{M}$ along which fracture, twinning, and/or amorphization is concentrated. In other words, the present simulations restrict inelastic mechanisms to a single twin system, and single plane for amorphization, and a single cleavage plane. For boron carbide, the plane for all such mechanisms is here taken as the basal plane of each crystal, as discussed in Sect. 3.5. It is understood that this idealized representation omits the real possibility of inelastic deformation and failure on other planes and in other directions in the crystal; for example, a very large number of conceivable inelastic deformation systems are reported in atomic simulations [6,7]. Consideration of all potential inelastic deformation and failure mechanisms (which would require introduction of additional components of $\boldsymbol{D}$ or more order parameters) exceeds current computational capabilities. The present simulations are thought to offer some insight into deformation and failure behavior of boron carbide polycrystals despite the aforementioned idealizations. As will be noted later, the overall strength of the polycrystals considered in the current simulations is thought to exceed that of real polycrystals due to the very small grain size [49] and restricted set of potential deformation and failure mechanisms available in the simulations.

Material behaviors and properties correspond to those of Sect. 3.5, with several additions. Firstly, the tangent elastic bulk modulus K is permitted to degrade with cumulative damage (i.e., with increasing ξ) for elastically tensile states, when $\mathrm{tr}\boldsymbol{\beta}^E > 0$, but maintains its full (initial) value under elastic compression. Secondly, the bulk and shear moduli retain small positive values, here 1% of their initial values, even at integration points within elements at which damage variable $\xi \to 1$, corresponding to zones or regions of the body termed herein as "failed". The equations governing such behaviors are identical to those used in [31,50] and are not repeated here. These features are necessary such that a compressed crystal, even if fractured, retains resistance to volume reduction (e.g., like a liquid) and prevent interpenetration of matter in failed zones. Finally, random initial lattice orientations corresponding to directions of cleavage and habit planes are assigned to each crystal, with two sets of orientations considered in forthcoming reported simulations. To enforce cleavage along the basal plane of each crystal, the parameter ϑ_ξ in (3.17) is assigned a value of 100, as in prior work [31,49,50].

Two different sets of deformation boundary conditions are considered, corresponding to pure shear and uniaxial (stress) compression. Pure shear, i.e., compression and tension applied in equal magnitudes along

perpendicular directions, is considered rather than simple shear as in Sect. 4 since simulations invoking simple shear were found to yield uninteresting solutions with failure behavior concentrated almost entirely at the boundaries of the domain. Let $\bar{\epsilon}$ denote the loading parameter that is incrementally increased as a simulation proceeds. For pure shear, boundary conditions on displacement are imposed as the updated spatial coordinates

$$y(X, 0, Z) = 0, \quad y(X, L, Z) = (1 - \bar{\epsilon})L; \qquad z(X, Y, 0) = 0, \quad z(X, Y, L) = (1 + \bar{\epsilon})L. \tag{5.1}$$

For uniaxial compression,

$$z(X, Y, 0) = 0, \quad z(X, Y, L) = (1 - \bar{\epsilon})L, \tag{5.2}$$

and the body is free to expand in lateral directions due to a positive Poisson's ratio and dilatation due to fracture, for example. For either case, free boundary conditions on the order parameters are imposed, i.e.,

$$\frac{\partial \psi}{\partial \nabla \xi} \cdot \boldsymbol{N} = 0, \quad \frac{\partial \psi}{\partial \nabla \eta} \cdot \boldsymbol{N} = 0 \qquad (\text{along } \partial \Omega_0), \tag{5.3}$$

with $\partial \Omega_0$ the external boundary of the aggregate with outward reference normal vector $\boldsymbol{N}$ in Cartesian space.

Results from twelve distinct simulations are reported later. Varied among simulations are the two aforementioned kinds of boundary conditions (shear or compression), two sets of initial lattice orientations (labeled 1 and 2), and three classes of material behavior. Regarding the latter, class one enables all three potential inelastic deformation mechanisms of Sect. 3: twinning, solid–solid phase changes (crystal to glass), and fracture. The second class enables twinning and fracture but not amorphization. Suppression of a particular inelastic mechanism is enforced by methods outlined in Sect. 3.5. The third class enables amorphization and fracture but not twinning. Twelve total simulations result from the space of 2 boundary condition types $\times$ 2 orientation sets $\times$ 3 material behavior classes.

Analysis of results is later aided by several definitions relating physical and mathematical variables. Let A and T denote local values of glass phase fraction and twin density, where

$$A(X, \bar{\epsilon}) = \eta(X, \bar{\epsilon}), \quad T(X, \bar{\epsilon}) = \min[\eta(X, \bar{\epsilon})/\eta_0, 1)]. \tag{5.4}$$

Average amorphous fraction, twin density, and damage for the polycrystal are then defined as the respective volume integrals

$$\bar{A}(\bar{\epsilon}) = \frac{1}{L^3} \int A(X, \bar{\epsilon}) \mathrm{d}\Omega_0, \qquad \bar{T}(\bar{\epsilon}) = \frac{1}{L^3} \int T(X, \bar{\epsilon}) \mathrm{d}\Omega_0, \qquad \bar{D}(\bar{\epsilon}) = \frac{1}{L^3} \int \xi(X, \bar{\epsilon}) \mathrm{d}\Omega_0. \tag{5.5}$$

The average shear stress for pure shear loading and the average normal stress for compressive loading, both positive in sign for the boundary conditions in (5.1) and (5.2), are defined, respectively, as

$$\bar{\tau}(\bar{\epsilon}) = \frac{1}{2L^3} \int [P^{ZZ}(X, \bar{\epsilon}) - P^{YY}(X, \bar{\epsilon})] \mathrm{d}\Omega_0, \qquad \bar{\sigma}(\bar{\epsilon}) = \frac{-1}{L^3} \int P^{ZZ}(X, \bar{\epsilon}) \mathrm{d}\Omega_0. \tag{5.6}$$

As a point of reference, recall that for a homogeneous isotropic linear elastic material, $\bar{\tau} = 2\mu\bar{\epsilon}$ and $\bar{\sigma} = E\bar{\epsilon}$ where $E = 9\mu K/(\mu + 3K)$ is the Young's modulus obtained from initial values of the elastic shear modulus μ and elastic bulk modulus K.

5.2 Simulation results

Model predictions obtained from FE simulations of deformation and failure of B_4C polycrystals are analyzed in what follows. Considered first are those six simulations invoking shear boundary conditions of (5.1). Results from the simulation with lattice orientation set 1 and all three mechanisms—fracture, twinning, and phase changes—enabled are shown in Fig. 7, corresponding to an applied strain of $\bar{\epsilon} = 0.08$. Contours of damage variable ξ are depicted in Fig. 7a. Highly damaged elements with $\xi > 0.8$ are removed from these and subsequent graphical images to aid viewing of cracks. The polycrystal is also rendered with intermediate transparency to allow for viewing of fields within, damage is rather diffuse in this simulation. Twin density T and glass fraction A of (5.4) are shown in respective Fig. 7b, c. In some regions, damage and coherent transformation zones are correlated, e.g., at the upper left corner, but in other regions there is less apparent correlation. Twins and glassy regions cut across multiple grains. Recall from Sect. 3 that the same order parameter η, with different ranges, is used to represent amorphization and twinning shear, where the latter

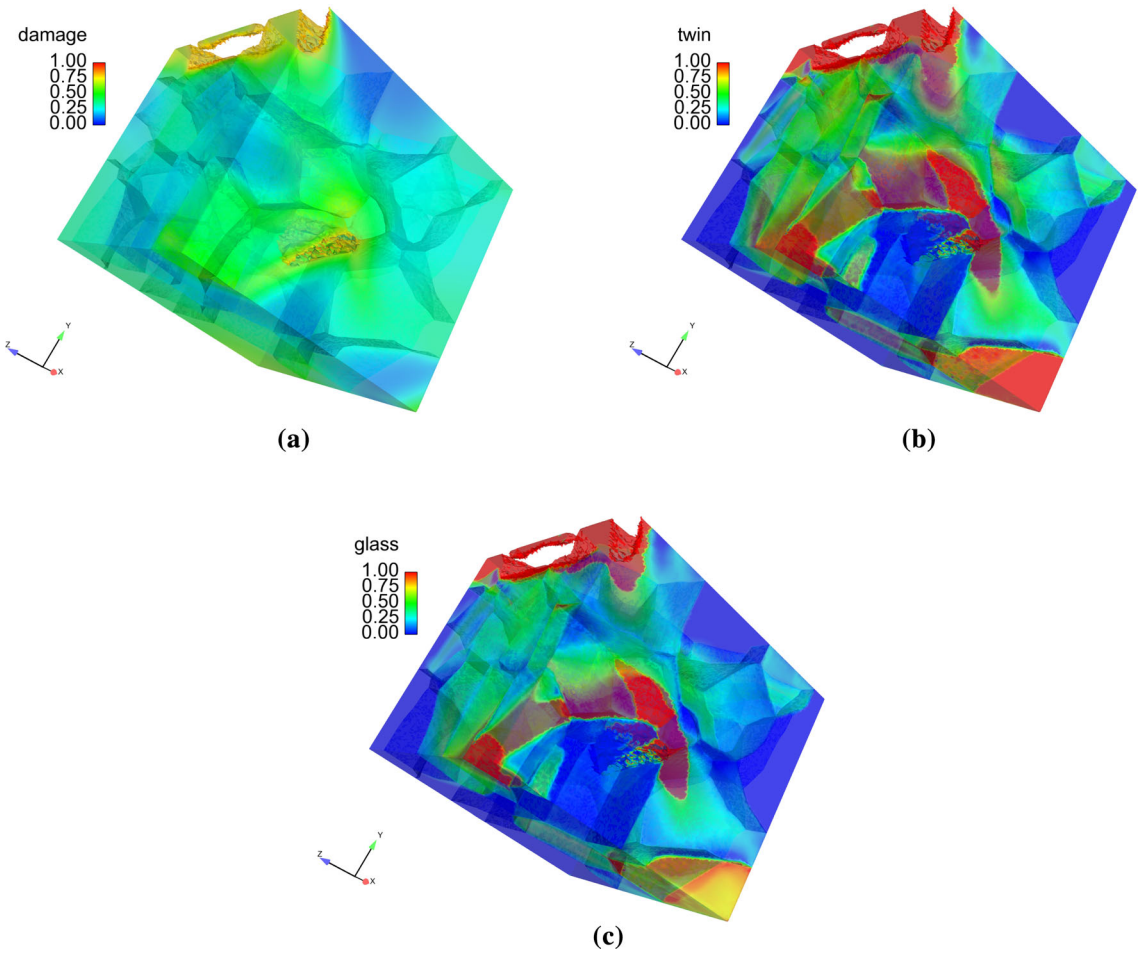

Fig. 7 Local field variables, shear, orientation set 1, $\bar{\epsilon} = 0.08$, all mechanisms enabled: **a** fracture parameter **b** twin density **c** glassy fraction

can also be interpreted as inelastic shear in a localized glassy band rather than twinning shear due to partial dislocations [12]. Thus, correlation of twinned and glassy regions is inevitable according to the present model implementation, where physically, a fully amorphous state has already undergone twinning, i.e., the sequence parent crystal to twinned crystal to glass has been completed at such a location in the deformed body.

Results for orientation set 1 and same strain level $\bar{\epsilon} = 0.08$, but with amorphization suppressed, are shown in Fig. 8. Damage in Fig. 8a is highly localized, with a dominant crack oriented diagonally along a plane of maximum shear stress. Twinning is concentrated along the crack boundary and at the lower right corner in Fig. 8b, which coincides with the heavily twinned zone in the lower right corner of Fig. 7b.

Results for orientation set 1 and same strain level $\bar{\epsilon} = 0.08$, but with twinning suppressed, are shown in Fig. 9. Damage in Fig. 9a is highly diffuse, similar in nature to that in Fig. 7a, but with crack locations differing among the two cases. Regions of glass are rather blocky, rather than band-like, in appearance and tend to encompass fully fractured zones.

Results from the simulation with lattice orientation set 2 and all three inelasticity mechanisms enabled are shown in Fig. 10, again corresponding to an applied strain of $\bar{\epsilon} = 0.08$. Contours of damage variable ξ are depicted in Fig. 10a. Damage is rather diffuse in this simulation, as was the case for its counterpart with lattice orientation set 1 in Fig. 7a, but crack locations and orientations differ among the two cases as a result of differing orientations of basal/cleavage planes. Twin density T and glass fraction A are shown in respective Fig. 10b, c. As was the case for Fig. 7, damage and transformation zones are positively correlated in some regions but not in others. Twins and glassy regions are often band-like and again traverse multiple crystals.

Results for orientation set 2 at $\bar{\epsilon} = 0.08$ and with amorphization suppressed are shown in Fig. 11. Damage in Fig. 11a is highly localized, with a dominant crack oriented diagonally along a plane of maximum shear stress;

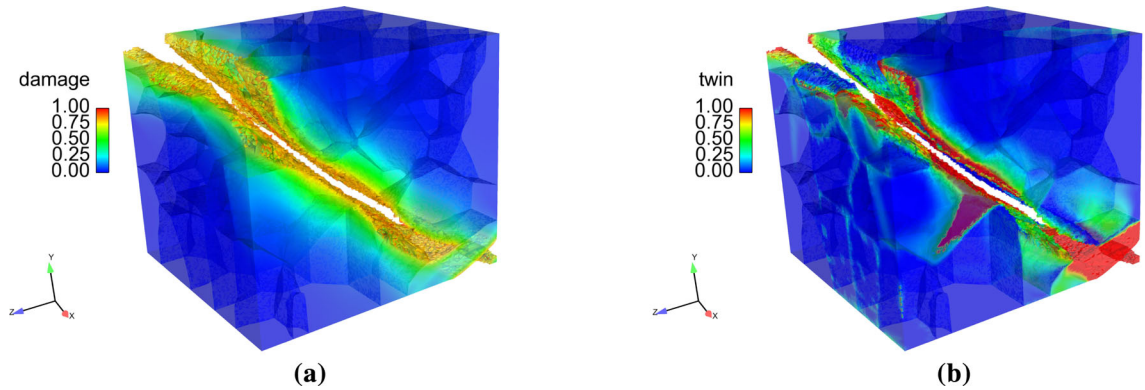

Fig. 8 Local field variables, shear, orientation set 1, $\bar{\epsilon} = 0.08$, amorphization suppressed: **a** fracture parameter **b** twin density

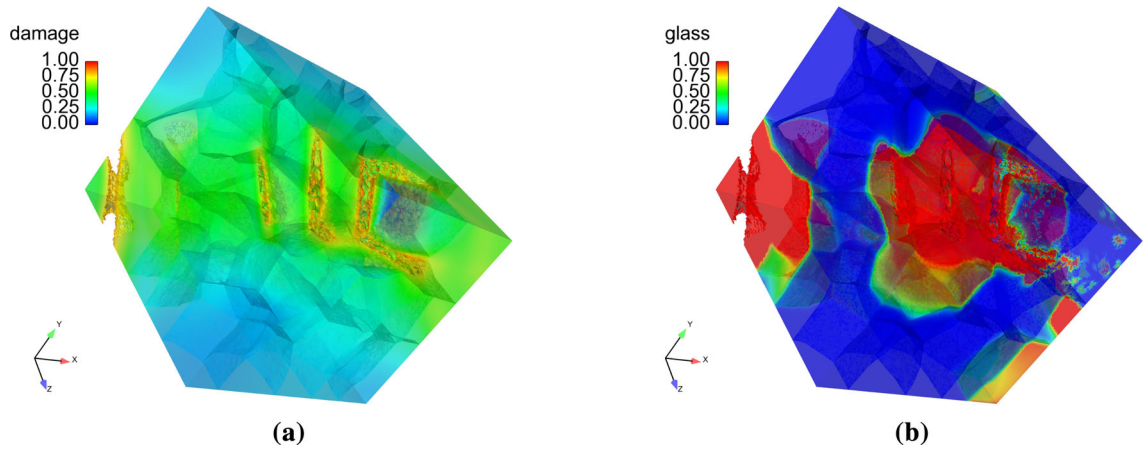

Fig. 9 Local field variables, shear, orientation set 1, $\bar{\epsilon} = 0.08$, twinning suppressed: **a** fracture parameter **b** glassy fraction

this is a similar trend, but with a differently oriented failure plane than that observed in the complementary simulation of Fig. 8. Twinning is scarce and is mostly concentrated along the crack boundary and at the upper right corner in Fig. 11b.

Results for orientation set 2 at the same strain level $\bar{\epsilon} = 0.08$, but with twinning suppressed, are shown in Fig. 12. Damage in Fig. 12a is diffuse, similar to that in Figs. 7a, 10a, but with fractured locations different among these cases. Regions of glass are either blocky or band-like and are widespread throughout the polycrystal.

Average shear stress of definition (5.6) and average structural variables of definitions in (5.5) are shown versus applied strain in Fig. 13 for the six cases invoking shear boundary conditions. Shear stress in Fig. 13a deviates from a perfectly linear elastic result, i.e., yielding corresponding to $\bar{\tau} < 2\mu\bar{\epsilon}$, at a global shear strain level between 1 and 2%. Peak shear stresses are similar among the six cases, attaining maximum values on the order of 6% of the initial shear modulus μ at strain levels on the order of 5%. Noteworthy are the severe stress drops experienced by the two cases with amorphization suppressed (i.e., labeled "glass and fracture"), results that correlate with development of localized large cracks evident in Figs. 8a and 11a. Post-peak average shear stresses decline less severely for the other cases in which damage is more diffuse.

Average fracture/damage parameter $\bar{D}$ is shown in Fig. 13b. Damage increases steadily after yielding for all cases, although its progression slows (i.e., lower slope) for the cases with amorphization suppressed. The slower growth of damage for these two cases correlates with formation of one or two large diagonal cracks as opposed to the diffuse damage observed in the other four simulations. Interestingly, an inverse correlation exists between average stress and average damage at applied strains exceeding 6%. This result emphasizes the importance of crack morphology and dominant flaws, the latter which evidently contribute much more to global stiffness loss than regions of diffuse microcracks. A similar finding was obtained from analysis of a

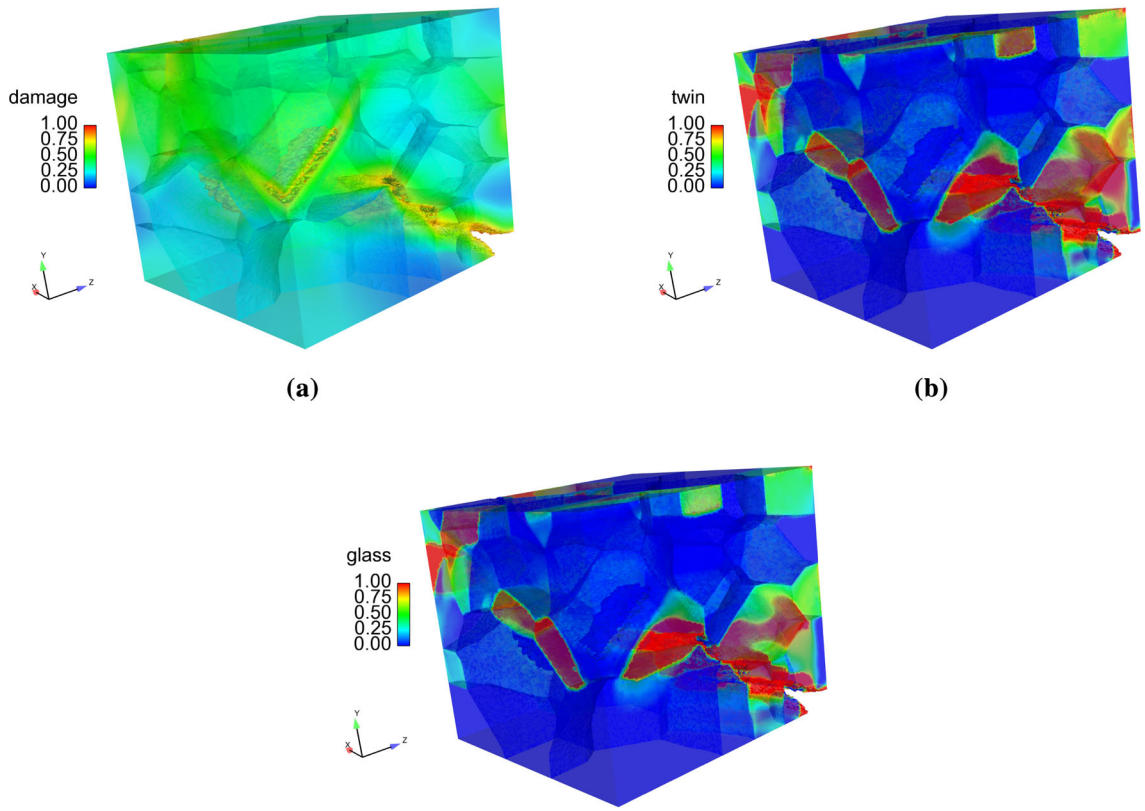

Fig. 10 Local field variables, shear, orientation set 2, $\bar{\epsilon} = 0.08$, all mechanisms enabled: **a** fracture parameter **b** twin density **c** glassy fraction

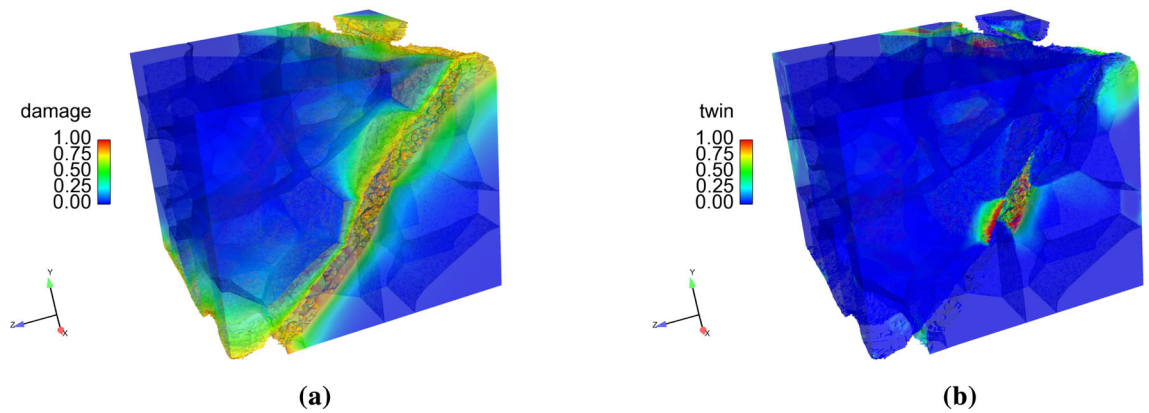

Fig. 11 Local field variables, shear, orientation set 2, $\bar{\epsilon} = 0.08$, amorphization suppressed: **a** fracture parameter **b** twin density

cohesive zone model of fracture, where defects of size small relative to the regularization length were found to not influence the peak global load supported by an elastic body with crack(s) [71].

Average twin density $\bar{T}$ is given in Fig. 13c. Behavior depends strongly on lattice orientation, with average twin density larger for set 1 than set 2. Upon achievement of peak stresses and emergence of localized fractured zones, twin densities for cases with glass disabled decrease with increasing applied load as a result of lower mechanical/elastic driving forces. This is possible in the model's numerical implementation (see Sect. 5.1) since local values of order parameter η that have not attained the threshold value of 0.9 are permitted to decrease with increasing load. Reversible twinning has been observed in some other kinds of (transparent)

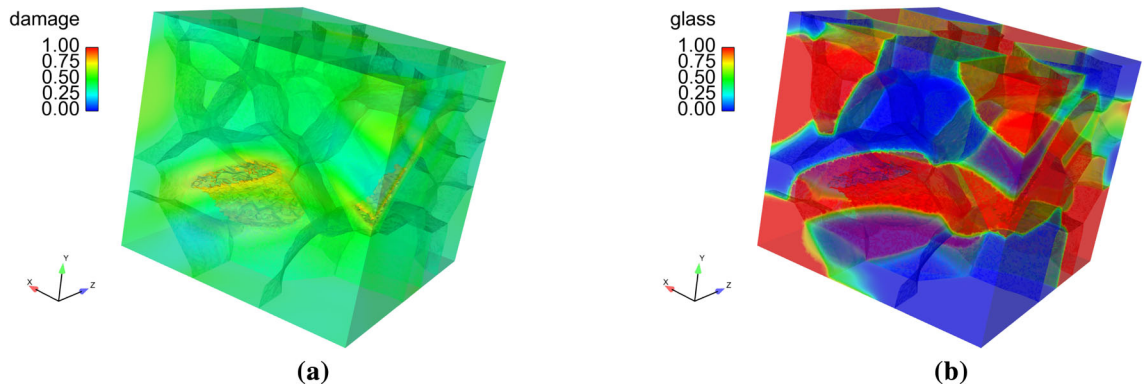

Fig. 12 Local field variables, shear orientation set 2, $\bar{\epsilon} = 0.08$, twinning suppressed: **a** fracture parameter **b** glassy fraction

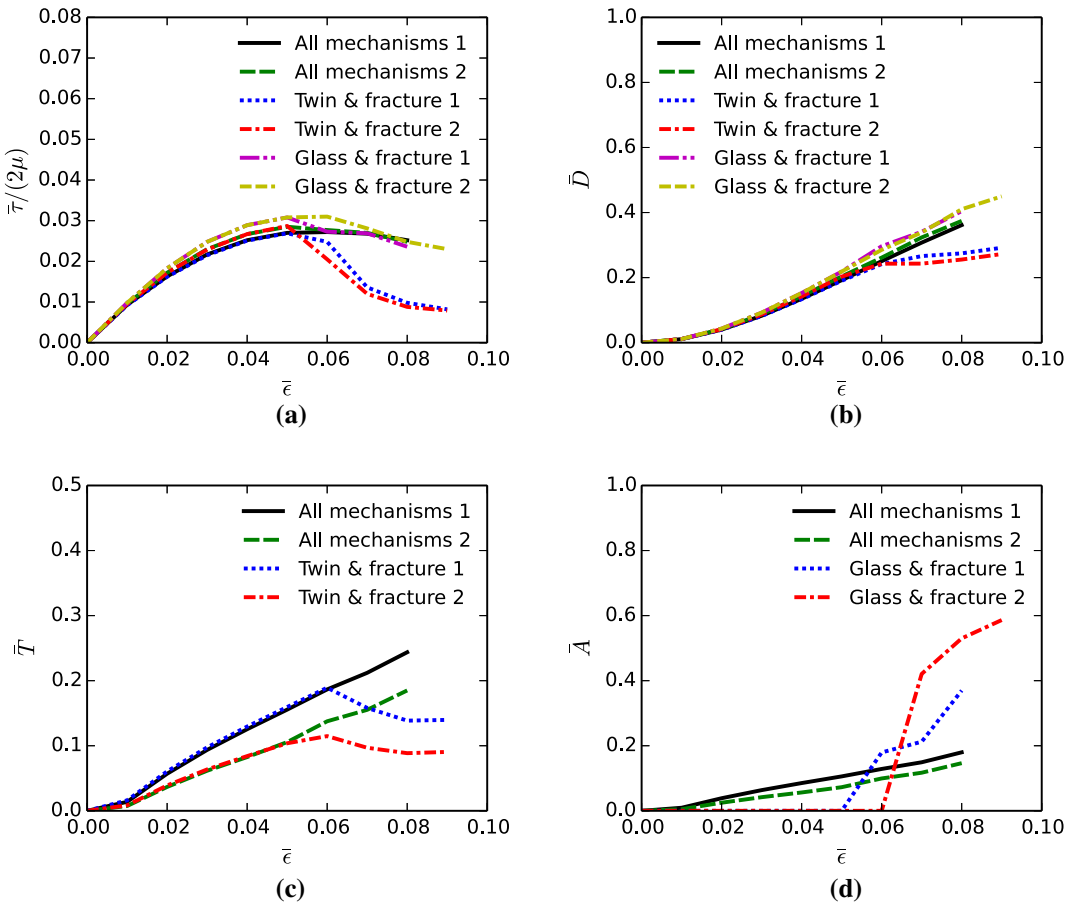

Fig. 13 Averaged field variables, shear, orientation sets 1 and 2: **a** shear stress **b** fracture parameter **c** twin density **d** glassy fraction

crystals such as calcite [37,66], though the possibility of reversible twinning or de-twinning in opaque boron carbide is uncertain.

Average amorphous fraction $\bar{A}$ is shown in Fig. 13d. The glass fraction increases rather slowly and steadily with increasing applied shear strain exceeding 1% for the two cases with all three mechanisms enabled, reaching maxima on the order of 1 or 2% at $\bar{\epsilon} = 0.08$. In contrast, for simulations with twinning suppressed, transformation behavior does not begin until applied strains on the order of 5 or 6% are reached; subsequently, increases in $\bar{A}$ are rapid and extreme, especially for orientation set 2 (see also Fig. 12b). Since such large volume fractions of glassy phase are not observed in experiments [1,2,10], it is concluded that suppression of inelastic

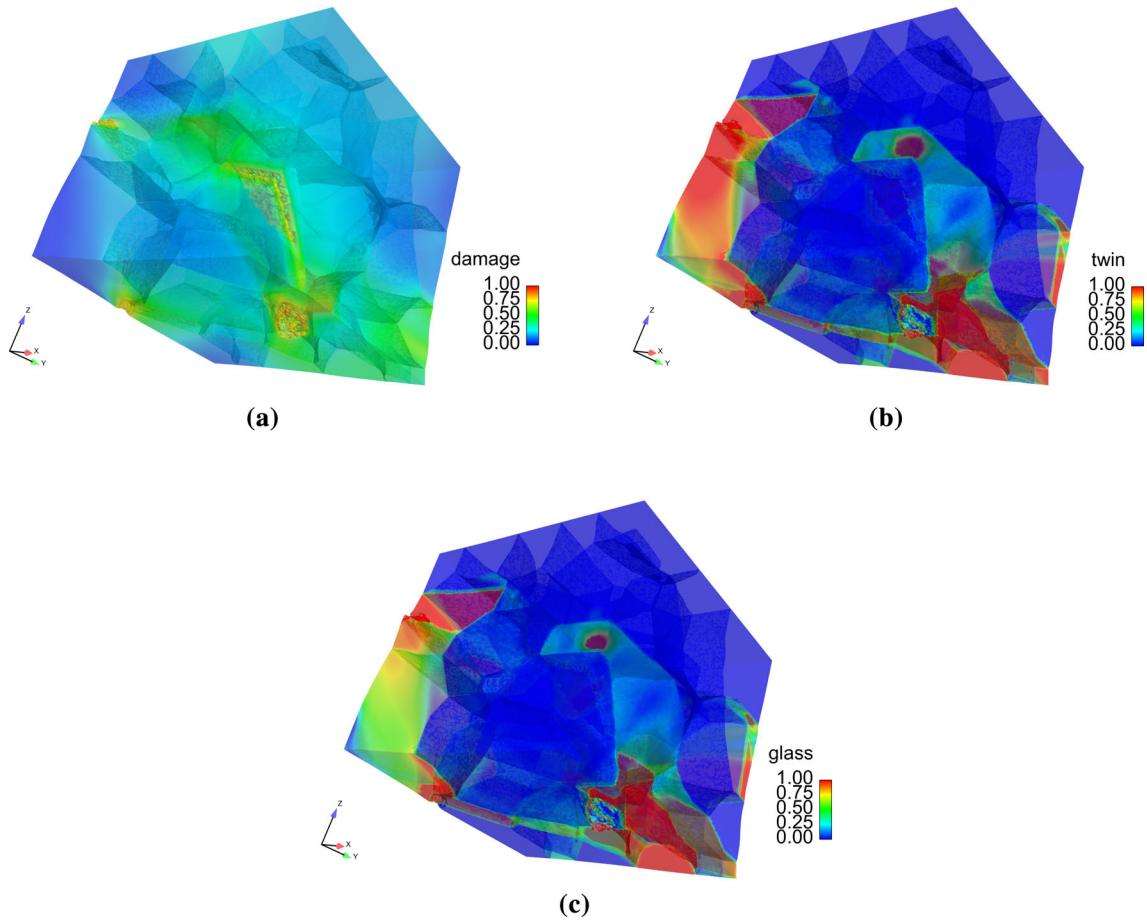

Fig. 14 Local field variables, compression, orientation set 1, $\bar{\epsilon} = 0.08$, all mechanisms enabled: **a** fracture parameter **b** twin density **c** glassy fraction

shear in the model gives physically unrealistic results. Rather, these predictions imply that inelastic shearing by twinning or by inclusion of shear bands accompanying transformation as in [47] should be incorporated in realistic continuum models of amorphization of boron carbide.

Collectively, these results also point to the possibility of increasing overall shear strength of the polycrystal and decreasing the tendency for localized fracture and localized shear failure if the inelastic shear accommodation by twins or glassy regions can be suppressed. Such a possibility is consistent with the recommendation for increasing resistance to failure under planar shock loading set forth in [47], based on parameter studies for semi-analytical homogeneous solutions. Polycrystalline resistance to shear deformation is thought to be a key metric of performance of ceramics in applications involving ballistic penetration [72–74].

Considered now are those six simulations invoking compression boundary conditions of (5.2). Results from the simulation with lattice orientation set 1 and all three inelasticity mechanisms, i.e., fracture, twinning, and phase changes, permitted, are shown in Fig. 14, at an applied axial compressive strain of $\bar{\epsilon} = 0.08$. Contours of damage variable ξ are given in Fig. 14a. Damage is rather diffuse in this simulation, similar to what was observed for shear boundary conditions in Figs. 7a and 10a. Twin density T and glass fraction A of (5.4) are depicted in Fig. 14b, c, respectively. As was the case for shear loading, in some regions damage and transformation zones are correlated, such as along the left edge, but in other regions there is less apparent correlation. Twinned zones and glassy regions cut across multiple grains. The green zone on the left side of Fig. 14c corresponds to material that has twinned but not yet (fully) transformed to glass.

Results for orientation set 1 at global compressive strain $\bar{\epsilon} = 0.08$ and with amorphization suppressed are shown in Fig. 15. Damage in Fig. 15a is mostly localized along a dominant shear-type crack, although some diffuse fractures are evident at the lower right side of the image. Twinning is concentrated along the left edge and lower right corner in Fig. 15b, both regions coinciding with the twinned zones evident in Fig. 14b.

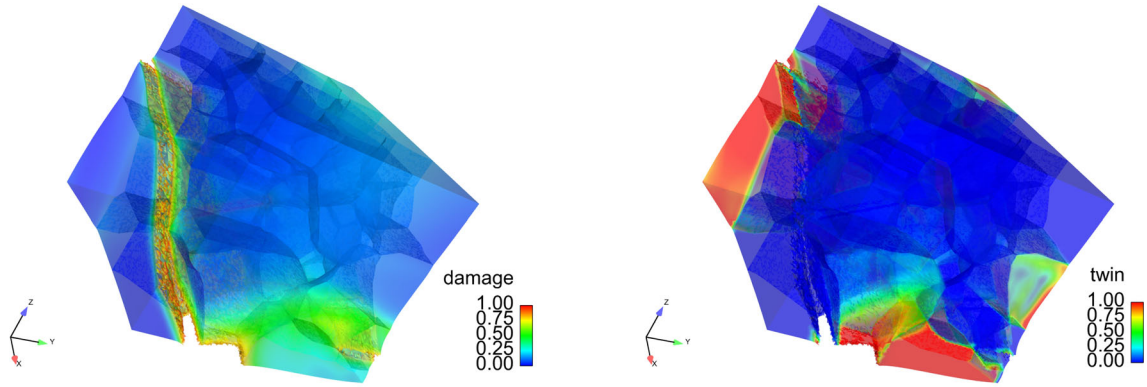

Fig. 15 Local field variables, compression, orientation set 1, $\bar{\epsilon} = 0.08$, amorphization suppressed: **a** fracture parameter **b** twin density

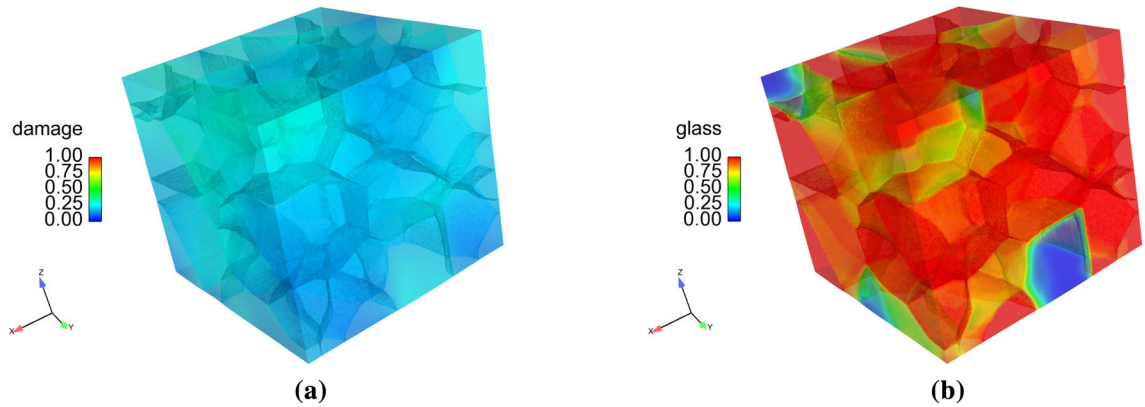

Fig. 16 Local field variables, compression, orientation set 1, $\bar{\epsilon} = 0.08$, twinning suppressed: **a** fracture parameter **b** glassy fraction

Results for orientation set 1 and $\bar{\epsilon} = 0.08$, but with twinning suppressed, are shown in Fig. 16. Damage in Fig. 16a is the most diffuse among all observed results, with no apparent localized fractures. Regions of glass are blocky and encompass a large fraction of the domain in Fig. 16b: in fact, the deformed body here consists of more glass than crystal.

Three other simulations with compression boundary conditions and orientation set 2 were analyzed, with inelasticity mechanisms enabled or suppressed analogously to the three simulations just described for orientation set 1. Contours of results demonstrate similar trends to those in Figs. 14, 15, and 16.

Average axial stress of definition (5.6), positive in compression, and average structural variables defined in (5.5) are shown versus applied compressive strain in Fig. 17 for all six cases invoking compression boundary conditions. Axial stress in Fig. 17a decreases relative to a perfectly linear elastic result, i.e., yielding corresponding to $\bar{\sigma} < E\bar{\epsilon}$, at an applied strain level between 1% and 2%. Peak stresses differ significantly among the six cases, attaining maximum values between of 2.5 and 4% of the initial tensile modulus E at global strain levels on the order of 7%.

Notable is a severe stress drops experienced by one of the two cases with amorphization suppressed (i.e., labeled "twin & fracture 1") correlating with the localized large crack evident in Fig. 15a. Stiffness reduction with increasing load is less rapid for the other cases wherein damage is more diffuse. Lattice orientation affects average stresses more here than what was observed in Fig. 13a for shear loading, the exception being the two cases with twinning suppressed. The latter two cases demonstrate very little softening at large strains corresponding to $\bar{\epsilon} \geq 0.07$.

A maximum stress of 4% of E corresponding to orientation set 1 (black curve in Fig. 17a) is approximately 18 GPa, very similar to the Hugoniot elastic limit (HEL) of the polycrystal determined from impact experiments [9,70,75]. However, the present numerical results correspond to uniaxial stress, quasi-static loading, nano-

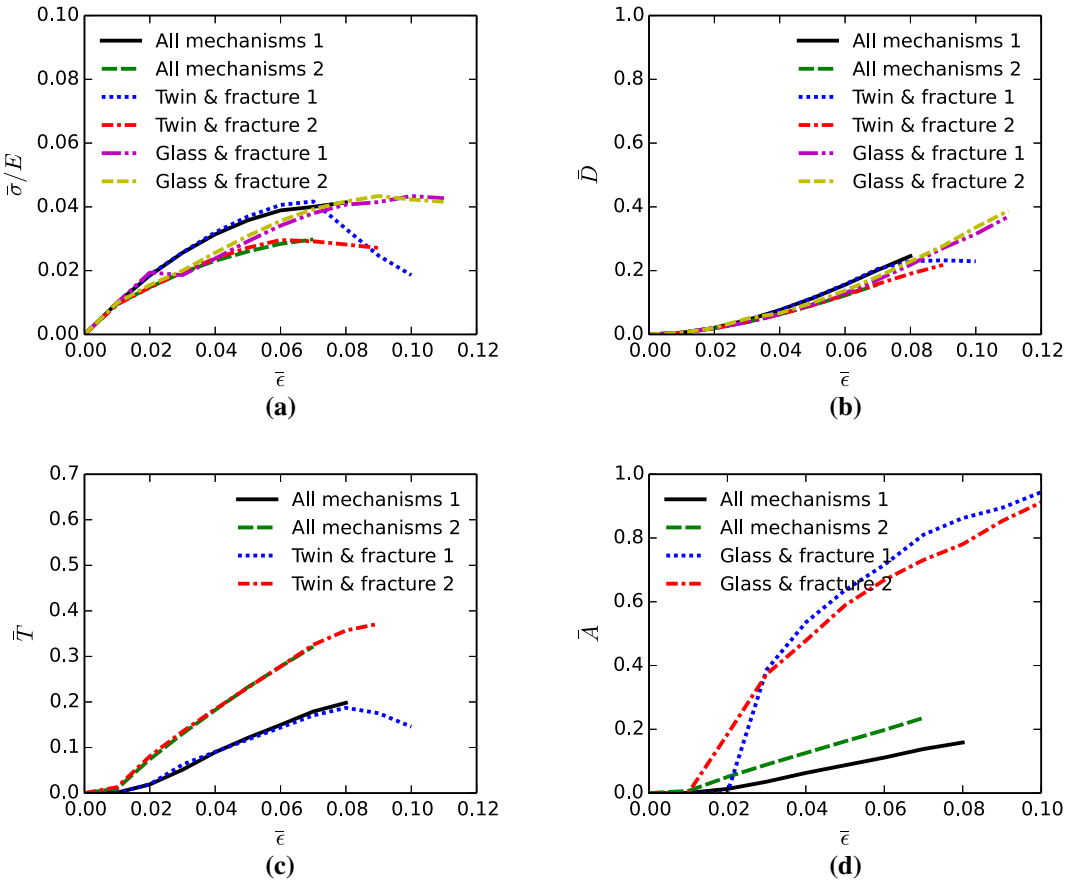

Fig. 17 Averaged field variables, compression, orientation sets 1 and 2: **a** axial stress **b** fracture parameter **c** twin density **d** glassy fraction

scale sized grains, and a restricted set of deformation mechanisms, e.g., a single twin system and fracture plane per crystal, with no grain boundary fracture. In contrast, the HEL is obtained for highly dynamic uniaxial strain loading, micron-scale sized grains, and potentially many more failure mechanisms. It is speculated that the smaller size and number of grains and the reduced number of inelasticity mechanisms result in greater strengths for the simulation results compared to unconfined (uniaxial stress) compression data from experiments. For example, the unconfined compressive strength of hot pressed polycrystalline boron carbide has been reported for specimens of dimensions of several mm as ranging from 3.5 to 4 GPa depending on loading rate from quasi-static to moderate rates achieved in a Kolsky bar apparatus [76].

Average fracture/damage parameter $\bar{D}$ is shown in Fig. 17b. Damage increases steadily after yielding for all cases, and its progression slows (i.e., lower slope) for orientation set 1 with amorphization suppressed. The latter results correlate with formation of a large diagonal crack apparent in Fig. 15a as opposed to the diffuse damage observed in other simulations. As was observed for shear loading, an inverse correlation exists between average stress and average damage, again highlighting the importance of dominant flaws over diffuse microcracks when considering the overall strength of a relatively brittle polycrystal.

Average twin density $\bar{T}$ is shown in Fig. 17c and demonstrates strong dependence on lattice orientation, as was the case for shear loading in Fig. 13c. However, here average twin density tends to be larger for orientation set 2 than set 1. The de-twinning behavior for orientation set 1 at large compressive strain follows a similar trend to that observed for some cases under shear loading.

Finally, average amorphous fraction $\bar{A}$ is shown in Fig. 17d. Some trends are similar to those reported for shear boundary conditions in the context of Fig. 13d. The glass fraction increases rather slowly and steadily with increasing applied shear strain exceeding 1% for the two cases with all three mechanisms enabled, again reaching maxima on the order of 1 or 2% by $\bar{\epsilon} = 0.08$. For the two simulations with twinning suppressed, transformation behavior begins sooner than observed for shear loading, at applied strains on the order of 1

or 2%. Subsequently, increases in $\bar{A}$ are rapid, extreme, and deemed unrealistically large (see Fig. 16b). As was the case for shear loading, these results confirm that suppression of inelastic shear in the model results in excessive phase transformation behavior. Instead, inelastic shearing by twinning or by inclusion of shear bands accompanying transformation as in [47] should be incorporated in continuum models of large deformation and failure of B_4C. Findings for static axial compression of polycrystals reported here are consistent with those of shear loading already discussed in the present work and for shock loading of single crystals discussed in [47]: suppression of inelastic shear accommodation by twins or glassy regions should lead to increased compressive strength and failure resistance.

5.3 Summary of results from polycrystal simulations

Important outcomes of the numerical (FE) results for B_4C are summarized in the points below:

- Localized damage zones more strongly influence failure behavior than diffuse microfractures, the latter leading to less severe tangent stiffness reduction than one or two dominant flaws;
- Inelastic shear accommodation by twinning or slippage in glassy bands leads to overall strength degradation and localized fractures;
- Elimination of the possibility of inelastic shearing by twinning or amorphization leads to unrealistically large volume fractions of glassy material;
- Lattice orientations tend to affect twinning behavior more strongly than they affect average damage or amorphous volume fractions;
- Similar trends are observed for pure shear loading and for uniaxial stress compression.

Perhaps most important in the context of design of boron-based ceramics for improved failure resistance [52,77], processing or alloying steps that would decrease the inelastic shear accommodation in twinned or amorphous regions should lead to more diffuse damage patterns and an increase in overall strength of the polycrystal, a conclusion also drawn from semi-analytical results reported for shock loading of single crystals in [47].

6 Conclusions

A novel geometrically nonlinear continuum theory has been developed to account for the physical mechanisms of elasticity, deformation twinning, solid–solid crystal-to-glass phase changes, and fracture in crystalline solids. These mechanisms are thought to occur sequentially, and in some cases simultaneously, in boron carbide ceramics. The theory has been specialized to consider inelastic deformation mechanisms on the basal plane in single crystals and polycrystals of this material. An analytical system of equations governing mechanical and transformation behavior has been derived and solved for simple shear deformations parallel to basal planes of a single crystal. Semi-analytical results demonstrate stresses for twin nucleation and subsequent failure similar in magnitude to those estimated from experiments or atomic simulations. A geometrically linearized version of the has been implemented in three-dimensional finite element simulations of compression or pure shear of polycrystalline microstructures. Numerical results demonstrate positive correlation between global strength and stiffness loss, nucleation and growth of large/dominant cracks, and inelastic shear deformation in band-like twinned or glassy regions that traverse multiple grains. Predicted compressive strengths exceed those observed in unconfined specimens of much larger dimensions with much larger grains. Future work should consider more potential inelasticity and failure mechanisms, e.g., other planes for shear localization or twinning as well as grain boundary fractures, that would tend to reduce predicted peak stresses.

References

1. Chen, M., McCauley, J.W., Hemker, K.J.: Shock-induced localized amorphization in boron carbide. Science **299**, 1563–1566 (2003)
2. Yan, X.Q., Tang, Z., Zhang, L., Guo, J.J., Jin, C.Q., Zhang, Y., Goto, T., McCauley, J.W., Chen, M.W.: Depressurization amorphization of single-crystal boron carbide. Phys. Rev. Lett. **102**, 075505 (2009)

3. Fanchini, G., McCauley, J.W., Chhowalla, M.: Behavior of disordered boron carbide under stress. Phys. Rev. Lett. **97**, 035502 (2006)
4. Taylor, D.E., McCauley, J.W., Wright, T.W.: The effects of stoichiometry on the mechanical properties of icosahedral boron carbide under loading. J. Phys. Condens. Matter. **24**, 505402 (2012)
5. Taylor, D.E.: Shock compression of boron carbide: a quantum mechanical analysis. J. Am. Ceram. Soc. **98**, 3308–3318 (2015)
6. An, Q., Goddard, W.A., Cheng, T.: Atomistic explanation of shear-induced amorphous band formation in boron carbide. Phys. Rev. Lett. **113**(9), 095501 (2014)
7. An, Q., Goddard, W.A.: Atomistic origin of brittle failure of boron carbide from large-scale reactive dynamics simulations: suggestions toward improved ductility. Phys. Rev. Lett. **115**, 105051 (2015a)
8. Grady, D.E.: Adiabatic shear failure in brittle solids. Int. J. Impact Eng. **38**, 661–667 (2011)
9. Clayton, J.D.: Towards a nonlinear elastic representation of finite compression and instability of boron carbide ceramic. Philos. Mag. **92**, 2860–2893 (2012a)
10. Clayton, J.D.: Mesoscale modeling of dynamic compression of boron carbide polycrystals. Mech. Res. Commun. **49**, 57–64 (2013)
11. Clayton, J.D., Tonge, A.: A nonlinear anisotropic elastic-inelastic constitutive model for polycrystalline ceramics and minerals with application to boron carbide. Int. J. Solids Struct. **64–65**, 191–207 (2015)
12. Li, Y., Zhao, Y.H., Liu, W., Zhang, Z.H., Vogt, R.G., Lavernia, E.J., Schoenung, J.M.: Deformation twinning in boron carbide particles within nanostructured Al 5083/B_4C metal matrix composites. Philos. Mag. **90**, 783–792 (2010)
13. Sano, T., Randow, C.L.: The effect of twins on the mechanical behavior of boron carbide. Metall. Mater. Trans. A **42**, 570–574 (2011)
14. Clayton, J.D.: Nonlinear Mechanics of Crystals. Springer, Dordrecht (2011)
15. Clayton, J.D., McDowell, D.L.: A multiscale multiplicative decomposition for elastoplasticity of polycrystals. Int. J. Plast. **19**, 1401–1444 (2003)
16. Kalidindi, S.R.: Incorporation of deformation twinning in crystal plasticity models. J. Mech. Phys. Solids **46**, 267–290 (1998)
17. Barton, N.R., Winter, N.W., Reaugh, J.E.: Defect evolution and pore collapse in crystalline energetic materials. Model. Simul. Mater. Sci. Eng. **17**, 035003 (2009)
18. Clayton, J.D.: A continuum description of nonlinear elasticity, slip and twinning, with application to sapphire. Proc. R. Soc. Lond. A **465**, 307–334 (2009)
19. Clayton, J.D.: Deformation, fracture, and fragmentation in brittle geologic solids. Int. J. Fract. **163**, 151–172 (2010a)
20. Clayton, J.D.: Modeling nonlinear electromechanical behavior of shocked silicon carbide. J. Appl. Phys. **107**, 013520 (2010b)
21. Aslan, O., Cordero, N.M., Gaubert, A., Forest, S.: Micromorphic approach to single crystal plasticity and damage. Int. J. Eng. Sci. **49**, 1311–1325 (2011)
22. Voyiadjis, G.Z., Kattan, P.I.: Damage Mechanics. CRC Press, Boca Raton (2005)
23. Bammann, D.J., Solanki, K.N.: On kinematic, thermodynamic, and kinetic coupling of a damage theory for polycrystalline material. Int. J. Plast. **26**, 775–793 (2010)
24. Xu, X.-P., Needleman, A.: Numerical simulations of fast crack growth in brittle solids. J. Mech. Phys. Solids **42**, 1397–1434 (1994)
25. Clayton, J.D.: Dynamic plasticity and fracture in high density polycrystals: constitutive modeling and numerical simulation. J. Mech. Phys. Solids **53**, 261–301 (2005)
26. Vogler, T.J., Clayton, J.D.: Heterogeneous deformation and spall of an extruded tungsten alloy: plate impact experiments and crystal plasticity modeling. J. Mech. Phys. Solids **56**, 297–335 (2008)
27. Foulk, J.W., Vogler, T.J.: A grain-scale study of spall in brittle materials. Int. J. Fract. **163**, 225–242 (2010)
28. Hou, T.Y., Rosakis, P., LeFloch, P.: A level-set approach to the computation of twinning and phase-transition dynamics. J. Comput. Phys. **150**, 302–331 (1999)
29. Del Piero, G., Lancioni, G., March, R.: A variational model for fracture mechanics: numerical experiments. J. Mech. Phys. Solids **55**, 2513–2537 (2007)
30. Kuhn, C., Müller, R.: A continuum phase field model for fracture. Eng. Fract. Mech. **77**, 3625–3634 (2010)
31. Clayton, J.D., Knap, J.: A geometrically nonlinear phase field theory of brittle fracture. Int. J. Fract. **189**, 139–148 (2014)
32. Weinberg, K., Hesch, C.: A high-order finite deformation phase-field approach to fracture. Contin. Mech. Thermodyn. **29**, 935–945 (2017)
33. Levitas, V.A., Levin, V.A., Zingerman, K.M., Freiman, E.I.: Displacive phase transitions at large strains: phase-field theory and simulations. Phys. Rev. Lett. **103**, 025702 (2009)
34. Clayton, J.D.: Phase field theory and analysis of pressure-shear induced amorphization and failure in boron carbide ceramic. AIMS Mater. Sci. **1**, 143–158 (2014a)
35. Schmitt, R., Kuhn, C., Müller, R.: On a phase field approach for martensitic transformations in a crystal plastic material at a loaded surface. Contin. Mech. Thermodyn. **29**, 957–968 (2017)
36. Clayton, J.D., Knap, J.: A phase field model of deformation twinning: nonlinear theory and numerical simulations. Phys. D **240**, 841–858 (2011a)
37. Clayton, J.D., Knap, J.: Phase field modeling of twinning in indentation of transparent single crystals. Model. Simul. Mater. Sci. Eng. **19**, 085005 (2011b)
38. Clayton, J.D., Knap, J.: Phase field analysis of fracture induced twinning in single crystals. Acta Mater. **61**, 5341–5353 (2013)
39. Hildebrand, F.E., Miehe, C.: A phase field model for the formation and evolution of martensitic laminate microstructure at finite strains. Philos. Mag. **92**, 4250–4290 (2012)
40. Padilla, C.A.H., Markert, B.: A coupled ductile fracture phase-field model for crystal plasticity. Contin. Mech. Thermodyn. **29**, 1017–1026 (2017)
41. Clayton, J.D.: Finsler geometry of nonlinear elastic solids with internal structure. J. Geom. Phys. **112**, 118–146 (2017a)

42. Saczuk, J.: Finslerian Foundations of Solid Mechanics. Zeszyty naukowe Instytutu Maszyn Przeplywowych Polskiej Akademii Nauk w Gdansku, Wydawnictwo IMP PAN, Gdansk (1996)
43. Stumpf, H., Saczuk, J.: A generalized model of oriented continuum with defects. Zeitschrift für Angewandte Mathematik und Mechanik (ZAMM) **80**, 147–169 (2000)
44. Clayton, J.D.: Finsler-geometric continuum mechanics. Technical Report ARL-TR-7694, US Army Research Laboratory, Aberdeen Proving Ground MD (2016a)
45. Clayton, J.D.: Generalized finsler geometric continuum physics with applications in fracture and phase transformations. Zeitschrift fur Angewandte Mathematik und Physik (ZAMP) 68, 9 (2017b)
46. Clayton, J.D.: Finsler-geometric continuum mechanics and the micromechanics of fracture in crystals. J. Micromech. Mol. Phys. **1**, 164003 (2016b)
47. Clayton, J.D.: Finsler-geometric continuum dynamics and shock compression. Int. J. Fract. **208**, 53–78 (2017c)
48. Clayton, J.D., Kraft, R.H., Leavy, R.B.: Mesoscale modeling of nonlinear elasticity and fracture in ceramic polycrystals under dynamic shear and compression. Int. J. Solids Struct. **49**, 2686–2702 (2012)
49. Clayton, J.D., Knap, J.: Phase field modeling of directional fracture in anisotropic polycrystals. Comput. Mater. Sci. **98**, 158–169 (2015a)
50. Clayton, J.D., Knap, J.: Phase field modeling of coupled fracture and twinning in single crystals and polycrystals. Comput. Methods Appl. Mech. Eng. **312**, 447–467 (2016)
51. An, Q., Goddard, W.A.: Boron suboxide and boron subphosphide crystals: hard ceramics that shear without brittle failure. Chem. Mater. **27**, 2855–2860 (2015b)
52. Subhash, G., Awasthi, A.P., Kunka, C., Jannotti, P., DeVries, M.: In search of amorphization-resistant boron carbide. Scr. Mater. **123**, 158–162 (2016)
53. Bejancu, A.: Finsler Geometry and Applications. Ellis Horwood, New York (1990)
54. Rund, H.: A divergence theorem for Finsler metrics. Monatshefte fur Mathematik **79**, 233–252 (1975)
55. Clayton, J.D.: Differential Geometry and Kinematics of Continua. World Scientific, Singapore (2014b)
56. Allen, S.M., Cahn, J.W.: A microscopic theory for antiphase boundary motion and its application to antiphase domain coarsening. Acta Metall. **27**, 1085–1095 (1979)
57. Levitas, V.I.: Phase field approach to martensitic phase transformations with large strains and interface stresses. J. Mech. Phys. Solids **70**, 154–189 (2014)
58. Clayton, J.D.: On anholonomic deformation, geometry, and differentiation. Math. Mech. Solids **17**, 702–735 (2012b)
59. Clayton, J.D., Bammann, D.J., McDowell, D.L.: Anholonomic configuration spaces and metric tensors in finite strain elastoplasticity. In. J. Non-Linear Mech. **39**, 1039–1049 (2004)
60. Weyl, H.: Space-Time-Matter, fourth edn. Dover, New York (1952)
61. Clayton, J.D., Bammann, D.J., McDowell, D.L.: A geometric framework for the kinematics of crystals with defects. Philos. Mag. **85**, 3983–4010 (2005)
62. Clayton, J.D., McDowell, D.L., Bammann, D.J.: Modeling dislocations and disclinations with finite micropolar elastoplasticity. Int. J. Plast. **22**, 210–256 (2006)
63. Tjahjanto, D.D., Turteltaub, S., Suiker, A.S.J.: Crystallographically based model for transformation-induced plasticity in multiphase carbon steels. Contin. Mech. Thermodyn. **19**, 399–422 (2008)
64. Clayton, J.D., Knap, J.: Nonlinear phase field theory for fracture and twinning with analysis of simple shear. Philos. Mag. **95**, 2661–2696 (2015b)
65. Takaki, T., Hasebe, T., Tomita, Y.: Two-dimensional phase-field simulation of self-assembled quantum dot formation. J. Crystal Growth **287**, 495–499 (2006)
66. Boiko, V.S., Garber, R.I., Kosevich, A.M.: Reversible Crystal Plasticity. AIP Press, New York (1994)
67. Hirth, J.P., Lothe, J.: Theory of Dislocations. Wiley, New York (1982)
68. Rice, J.R.: Mathematical analysis in the mechanics of fracture. In: Liebowitz, H. (ed.) Fracture: An Advanced Treatise, pp. 191–311. Academic Press, New York (1968)
69. Beaudet, T.D., Smith, J.R., Adams, J.W.: Surface energy and relaxation in boron carbide $(10\bar{1}1)$ from first principles. Solid State Communications **219**, 43–47 (2015)
70. Dandekar, D. P.: Shock response of boron carbide. Technical Report ARL-TR-2456, US Army Research Laboratory, Aberdeen Proving Ground MD (2001)
71. Ferdjani, H., Abdelmoula, R., Marigo, J.-J.: Insensitivity to small defects of the rupture of materials governed by the Dugdale model. Contin. Mech. Thermodyn. **19**, 191–210 (2007)
72. Bourne, N.K.: The relation of failure under 1D shock to the ballistic performance of brittle materials. Int. J. Impact Eng. **35**, 674–683 (2008)
73. Clayton, J.D.: Penetration resistance of armor ceramics: dimensional analysis and property correlations. Int. J. Impact Eng. **85**, 124–131 (2015)
74. Clayton, J.D.: Dimensional analysis and extended hydrodynamic theory applied to long-rod penetration of ceramics. Def. Technol. **12**, 334–342 (2016c)
75. Vogler, T.J., Reinhart, W.D., Chhabildas, L.C.: Dynamic behavior of boron carbide. J. Appl. Phys. **95**, 4173–4183 (2004)
76. Paliwal, B., Ramesh, K.T.: Effect of crack growth dynamics on the rate-sensitive behavior of hot-pressed boron carbide. Scr. Mater. **57**, 481–484 (2007)
77. Tang, B., An, Q., Goddard, W.A.: Improved ductility of boron carbide by microalloying with boron suboxide. J. Phys. Chem. C **119**, 24649–24656 (2015)